



1 **BioRT-Flux-PIHM v1.0: a watershed biogeochemical reactive transport**  
2 **model**

3 Wei Zhi<sup>1</sup>, Yuning Shi<sup>2</sup>, Hang Wen<sup>1</sup>, Leila Saberi<sup>3</sup>, Gene-Hua Crystal Ng<sup>3</sup>, Li Li<sup>1,\*</sup>

4 <sup>1</sup> Department of Civil and Environmental Engineering, The Pennsylvania State University, State  
5 College, PA 16802, USA

6 <sup>2</sup> Department of Ecosystem Science and Management, The Pennsylvania State University, State  
7 College, PA 16802, USA

8 <sup>3</sup> Department of Earth Sciences, University of Minnesota, Twin Cities, MN 55455, USA

9 \* Correspondence to [lili@engr.psu.edu](mailto:lili@engr.psu.edu)



10

## Abstract

11 Watersheds are the fundamental Earth surface functioning unit that connects the land to  
12 aquatic systems. Existing watershed-scale models typically have physics-based  
13 representation of hydrology process but often lack mechanism-based, multi-component  
14 representation of reaction thermodynamics and kinetics. This lack of watershed reactive  
15 transport models has limited our ability to understand and predict solute export and water  
16 quality, particularly under changing climate and anthropogenic conditions. Here we  
17 present a recently developed BioRT-Flux-PIHM (BFP) v1.0, a watershed-scale  
18 biogeochemical reactive transport model. Augmenting the previously developed RT-Flux-  
19 PIHM that integrates land-surface interactions, surface hydrology, and abiotic  
20 geochemical reactions (Bao et al., 2017, WRR), the new development enables the  
21 simulation of 1) biotic processes including plant uptake and microbe-mediated  
22 biogeochemical reactions that are relevant to the transformation of organic matter that  
23 involve carbon, nitrogen, and phosphorus; and 2) shallow and deep water partitioning to  
24 represent surface and groundwater interactions. The reactive transport part of the code  
25 has been verified against the widely used reactive transport code CrunchTope. BioRT-  
26 Flux-PIHM v1.0 has recently been applied to understand reactive transport processes in  
27 multiple watersheds across different climate, vegetation, and geology conditions. This  
28 paper introduces the governing equations and model structure of the code. It also  
29 demonstrates examples that simulate shallow and deep water interactions, and  
30 biogeochemical reactive transport relevant to nitrate and dissolved organic carbon (DOC).  
31 These examples were illustrated in two simulation modes of varying complexity. One is  
32 the spatially implicit mode that focuses on processes and average behavior of a  
33 watershed. Another is in a spatially explicit mode that includes details of topography, land  
34 cover, and soil property conditions. The spatially explicit mode can be used to understand  
35 the impacts of spatial structure and identify hot spots of biogeochemical reactions.



## 36 1. Introduction

37 Watersheds are the fundamental Earth surface units that receive and process  
38 water, mass, and energy (Li, 2019). Watershed processes include land-surface  
39 interactions that regulate evapotranspiration and discharge, and water partitioning  
40 between shallow soil lateral flow going into streams versus downward and recharge into  
41 the deeper subsurface (Figure 1). Complex biogeochemical interactions also occur  
42 between soil, water, roots, and microbe, dictating the CO<sub>2</sub> effluxes via soil respiration,  
43 export of soil weathering and biotransformation, and nutrient cycling (Fatichi et al.,  
44 2019;van der Velde et al., 2010).

45 These hydrological and biogeochemical processes determine how Earth surface  
46 responds to external forcings such as hydroclimatic drivers and human perturbations (van  
47 der Velde et al., 2014;Miller et al., 2020;Han et al., 2019;Steimke et al., 2018).  
48 Understanding these processes remain challenging due to the complex coupling of land  
49 surface, hydrology, and biogeochemical reactions (Kirchner, 2003). An example is the  
50 concentration-discharge (C-Q) relationships of solutes at stream and river outlets. These  
51 relationships encode integrated signature of Earth surface response to changes in  
52 hydrological conditions. Similar C-Q relationships have been observed for some solutes  
53 across watersheds under diverse geology and climate conditions (Godsey et al.,  
54 2009;Basu et al., 2010;Moatar et al., 2017;Zarnetske et al., 2018), whereas different  
55 solutes have shown contrasting patterns in the same watershed (Miller et al.,  
56 2017;Herndon et al., 2015;Zhi et al., 2019;Musolff et al., 2015). A general theory that can  
57 explain contrasting observations under diverse watershed characteristics and forcing  
58 conditions remains elusive. The lack of understanding of mechanisms that govern  
59 hydrological and biogeochemical interactions presents major roadblocks for forecasting  
60 water quality such that water issues such as eutrophication persist worldwide.

61 One of the challenges along these lines is the lack of modeling tools that  
62 mechanistically link hydrological and biogeochemical processes at the watershed scale.  
63 Model development has been advancing primarily within the disciplinary boundaries of  
64 hydrology and biogeochemistry (Li, 2019). Hydrology models that focus on solving for  
65 water storage and fluxes at the watershed scale and beyond (Fatichi et al., 2016), and



66 reactive transport models (RTMs) that center on aqueous and solid concentration  
67 changes arising from transport and multi-component biogeochemical reactions typically  
68 in “closed” groundwater systems without much interactions with “open” watersheds  
69 directly receiving precipitation and sunlight (Steeffel et al., 2015;Li et al., 2017b;Mayer et  
70 al., 2002;MacQuarrie and Mayer, 2005). This comes along with a history of hydrologists  
71 often trained as physicists studying fluid mechanics, and biogeochemists typically grow  
72 up as geologists, chemists, or environmental engineers.

73 Recent works have shown some integration across these two lines. Examples  
74 include HSPF (Hydrological Simulation Program – FORTRAN) (Filoso et al.,  
75 2004;Laroche et al., 1996), SWAT (Soil & Water Assessment Tool) (Gassman et al.,  
76 2007;Lam et al., 2010;Moriassi et al., 2013;Neitsch et al., 2011), CATHY (Catchment  
77 Hydrology) (Gatel et al., 2019;Scudeler et al., 2016), PAWS (Process-based Adaptive  
78 Watershed Simulator) (Niu and Phanikumar, 2015;Qiu et al., 2019). These models have  
79 relatively crude representations of solute leaching out of element bulk mass as part of the  
80 solute export. These models do not represent kinetics and thermodynamics of multi-  
81 component biogeochemical reactions typically done in reactive transport models (RTMs).  
82 In filling in this model development need, recently we developed the watershed reactive  
83 transport code RT-Flux-PIHM that integrates kinetics and thermodynamics of multi-  
84 component geochemical reactions with the land-surface and hydrology model Flux-PIHM  
85 (Bao et al., 2017). The geochemical reactions in RT-Flux-PIHM are abiotic, including  
86 mineral dissolution and precipitation, aqueous and surface complexation, and ion  
87 exchange reactions.

88 This manuscript introduces BioRT-Flux-PIHM (BFP) v1.0, augmented based on  
89 RT-Flux-PIHM with two additions. One is the capability of simulating biotic processes  
90 including plant uptake of nutrients, and microbe-mediated reactions in the soil. These soil  
91 processes include the transformation of fresh and old organic matter, for example, soil  
92 respiration that produces CO<sub>2</sub> and dissolved organic carbon (DOC), and nutrient cyclings  
93 such as nitrification and denitrification. The other is the introduction of a deeper layer  
94 below the shallow soil that enables the simulation of interactions of deep water and  
95 shallow soil water flow (Figure 1). Here the deep water is loosely defined as the water  
96 beyond the soil zone, typically in less weathered, fractured subsurface that harbors the



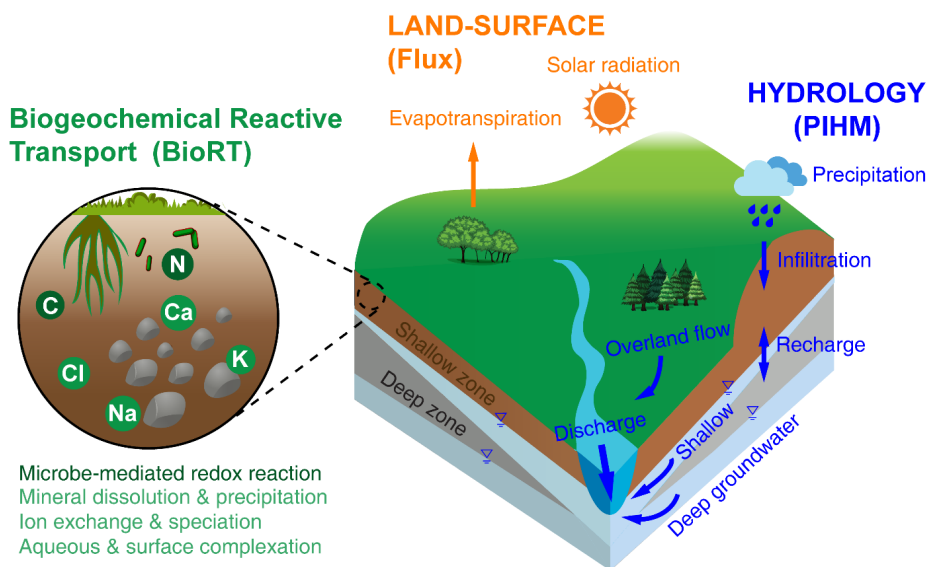
97 relatively old and slow-moving groundwater contributing to streams. This contrasts the  
98 shallow water in highly permeable soils. Mounting evidence in recent years has shown  
99 that the deeper water beyond the shallow soil interacts with streams, brings water with  
100 distinct chemistry, sustains base flow in dry times, and buffers climate variability (Gurdak,  
101 2017;Green, 2016;Taylor et al., 2013;Condon et al., 2013;Anyah et al., 2008;Maxwell et  
102 al., 2011;Gleeson et al., 2015). They are therefore a fundamental component of the  
103 hydrologic cycle and water budget. The groundwater-surface water interactions also  
104 modulate land-atmospheric energy exchanges and soil moisture dynamics. Including the  
105 deep water component therefore enables the simulation of such interactions and the  
106 dynamics of water quality.

107 This paper introduces the governing equations, model structure and capabilities of  
108 BFP. The biogeochemical reactive transport code has been verified against the widely  
109 used reactive transport code CrunchTope (Supporting Information). We showcase the  
110 model using two examples of varying complexity: one on nitrate processes run in a  
111 spatially implicit mode; another on the production and transport of dissolved organic  
112 carbon (DOC) in a spatially explicit mode with representation of spatial details. The source  
113 code and the examples shown here are hosted in the Github page  
114 (<https://github.com/PSUmodeling/BioRT-Flux-PIHM>).

## 115 **2. Model description**

116 BioRT-Flux-PIHM integrates different processes in three modules (Figure 1). The  
117 Flux module is for land-surface interaction processes including surface energy balance,  
118 solar radiation, and evapotranspiration (ET) (Shi et al., 2013). The hydrology module  
119 PIHM simulates water processes including precipitation, interception, infiltration,  
120 recharge, surface runoff, subsurface lateral flow, and deep water flow (Qu and Duffy,  
121 2007). The BioRT module is for multi-component biogeochemical reactive transport  
122 processes including microbe-mediated redox reactions (e.g., carbon decomposition and  
123 nutrient transformation), ion exchange, aqueous and surface complexation, and mineral  
124 dissolution and precipitation.

125



126

127 **Figure 1.** A conceptual diagram for processes at the watershed scale. This includes surface land  
128 interactions such as solar radiation, evapotranspiration); hydrological processes partitioning water  
129 between surface runoff, shallow soil water lateral flow, and deeper water entering the stream; and  
130 soil biogeochemical reactions including abiotic reactions (e.g., mineral dissolution and  
131 precipitation, ion exchange, surface complexations), and microbe-mediated reactions such as the  
132 transformation of carbon and nitrogen. These processes are represented in three modules: the  
133 Flux module for land-surface interaction processes, the PIHM module for hydrology processes,  
134 and the recently augmented BioRT module for soil biogeochemical reaction processes.  
135 Conceptually the shallow water zone includes the shallow subsurface such as soil and weathered  
136 zone that are more conducive to water flow (e.g., lateral flow or interflow). The deep zone refers  
137 to the less weathered, fractured zone that harbors the relatively old and slow flowing water that  
138 contributes to stream flow. Reactions can occur in both shallow and deep zones.

139

140 The land surface and hydrology modules are coupled to solve for temperature and  
141 water storage, from which water fluxes can be quantified for surface runoff, shallow and  
142 deep water fluxes. The BioRT module uses calculated temperature, water storage, and  
143 fluxes to simulate advection, diffusion / dispersion, and biogeochemical reactions in both  
144 shallow and deep zones. The reactions can be kinetics-controlled or thermodynamically  
145 controlled (e.g., ion exchange, surface complexation (sorption), and aqueous  
146 complexation). Users can define the type of reactions to be included and the form of

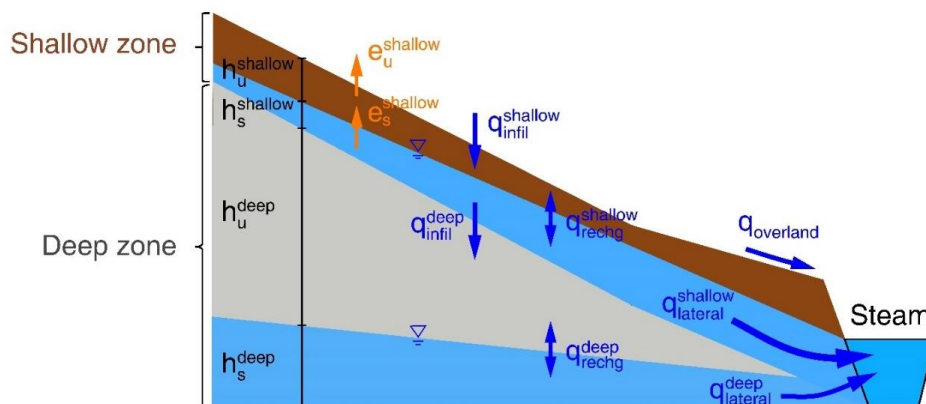


147 reaction kinetics in the input files. The output of BioRT includes the time series of aqueous  
148 and solid concentrations in shallow and deep zones and in stream water.

149 The simulation domain can be discretized into prismatic grids based on  
150 topography. Each grid is partitioned into surface and shallow and deep subsurface layers.  
151 The shallow subsurface is loosely defined as the highly permeable subsurface that are  
152 most conductive to water flow, contrasting the deep zone that is broadly defined as the  
153 lower permeability zone beyond the shallow zone. In many places, this shallow zone is  
154 the soil zone that is most conductive to water flow (e.g., lateral flow) and is very  
155 responsive to hydroclimatic forcing. The deep subsurface zone is the less weathered,  
156 fractured layer that harbors the relatively old and slow flowing water that contributes to  
157 stream flow. Note that these definitions differ from those in the hydrology community,  
158 which often refer to the shallow soil water flow as groundwater, in a way that distinguishes  
159 from the surface runoff (Winter et al., 1998;Dingman, 2015;Todd and Mays, 2005). As  
160 illustrated in Figure 1, both shallow and deep zone have unsaturated and saturated  
161 layers, enabling the simulation of the “two water tables” (Brantley et al., 2017). These  
162 transient water tables have been observed in catchments of Shale Hills, Garner Run, and  
163 Cole Farm (Li et al., 2018;Brantley et al., 2018).

164

### 165 3. Governing equations



166

167 **Figure 2.** Hillslope view of the shallow and deep zones and relevant water flows. The symbol of  
168 “h”, “e”, and “q” denotes water head, evapotranspiration, and water flow, respectively. The



169 subscript letter “u” and “s” refers to unsaturated and saturated layer, respectively. Detailed  
 170 equations are listed in the following sections.

171

### 172 3.1 The water equations in shallow and deep zones

173 As shown in Figure 2, in each prismatic element, the shallow zone has unsaturated  
 174 and saturated water storages and interactions between the two storages:

$$175 \quad \theta^{shallow} \frac{dh_u^{shallow}}{dt} = q_{infil}^{shallow} - q_{rechg}^{shallow} - e_u^{shallow} \quad (1)$$

$$176 \quad \theta^{shallow} \frac{dh_s^{shallow}}{dt} = q_{rechg}^{shallow} - q_{infil}^{deep} - e_s^{shallow} + \sum_{ij}^1 q_{lateral\_ij}^{shallow} \quad (2)$$

177 Where  $h_u^{shallow}$  and  $h_s^{shallow}$  are the unsaturated and saturated water storage in the  
 178 shallow zone, respectively;  $\theta^{shallow}$  is the shallow zone porosity;  $q_{infil}^{shallow}$  and  $q_{infil}^{deep}$   
 179 are the shallow and deep infiltration from the surface to the shallow zone and from the shallow  
 180 to the deep zone, respectively;  $q_{rechg}^{shallow}$  and  $q_{rechg}^{deep}$  are the recharge from the unsaturated  
 181 layer to the saturated layer in the shallow and deep zones, respectively;  $e_u^{shallow}$  and  
 182  $e_s^{shallow}$  are shallow evapotranspiration from the unsaturated and saturated layer (Shi,  
 183 2012), respectively;  $q_{lateral\_ij}^{shallow}$  is the shallow normalized lateral flux in the saturated layer  
 184 from element  $i$  to its neighbor  $j$  ( $\leq 3$ ).

185 Infiltration and recharge fluxes in the shallow zone for the elements  $i$  are calculated  
 186 using the Richards equation, in which hydraulic water head  $H$  (i.e., the summation of  
 187 water storage  $h$  and elevation head  $z$ ) and hydraulic conductivity  $K$  determine the fluxes:

$$188 \quad q_{infil}^{shallow} = AK_{infil}^{shallow} \frac{H_{sur} - H_u^{shallow}}{D_{inf}} \quad (3)$$

$$189 \quad q_{rechg}^{shallow} = AK_{effV}^{shallow} \frac{H_u^{shallow} - H_s^{shallow}}{0.5D_{shallow}} \quad (4)$$

190 Where  $A$  is the element area in the vertical direction;  $D_{inf}$  and  $D_{shallow}$  are the  
 191 thickness of infiltration (0.1 m) and shallow layer, respectively;  $K_{infil}^{shallow}$  and  $K_{effV}^{shallow}$   
 192 are the infiltration and effective hydraulic conductivity in the vertical direction in the shallow





193 zone, respectively;  $H_{sur}$  is the surface hydraulic water head ( $= h_{sur} + z_{sur}$ );  $H_u^{shallow}$  and  
 194  $H_s^{shallow}$  are the shallow hydraulic water head in the unsaturated and saturated layer,  
 195 respectively. Shallow lateral flow in the saturated layer is calculated using Darcy's law:

$$196 \quad q_{lateral\_ij}^{shallow} = A_{ij} K_{effH\_ij}^{shallow} \frac{(H_s^{shallow})_i - (H_s^{shallow})_j}{D_{ij}} \quad (5)$$

197 Where  $A_{ij}$  is the projection area of the saturated layer between elements  $i$  and  $j$ ;  $D_{ij}$  is  
 198 the distance between the centers of elements  $i$  and  $j$ ;  $K_{effH\_ij}^{shallow}$  is the harmonic mean of  
 199 shallow effective hydraulic conductivity in the horizontal direction ( $K_{effH}^{shallow}$ ) between  
 200 elements  $i$  and  $j$ . The interaction between the shallow saturated zone and stream channel  
 201 also follows the Eq. (5), where the adjacent head is replaced by the level of the channel  
 202 water.

203 Similar to the shallow zone, the deep zone in each element  $i$  can have unsaturated  
 204 and saturated storages, with unsaturated-saturated flow within  $i$ :

$$205 \quad \theta^{deep} \frac{dh_u^{deep}}{dt} = q_{infil}^{deep} - q_{rechg}^{deep} \quad (6)$$

$$206 \quad \theta^{deep} \frac{dh_s^{deep}}{dt} = q_{rechg}^{deep} + \sum_j^1 q_{lateral\_ij}^{deep} \quad (7)$$

207 Where  $h_u^{deep}$  and  $h_s^{deep}$  are the unsaturated and saturated storages in the deep zone,  
 208 respectively;  $\theta^{deep}$  is the deep zone porosity;  $q_{rechg}^{deep}$  is the deep recharge flux from the  
 209 unsaturated layer to the saturated layer;  $q_{lateral\_ij}^{deep}$  is the deep normalized lateral flux from  
 210 element  $i$  to its neighbor  $j$  ( $\leq 3$ ).

211 Deep lateral flow is calculated using Darcy's law:

$$212 \quad q_{lateral\_ij}^{deep} = A_{ij} K_{effH\_ij}^{deep} \frac{(H_s^{deep})_i - (H_s^{deep})_j}{D_{ij}} \quad (8)$$

213 Where  $H_s^{deep}$  is the deep hydraulic water head;  $K_{effH\_ij}^{deep}$  is the harmonic mean of the deep  
 214 effective hydraulic conductivity in the horizontal direction ( $K_{effH}^{deep}$ ) between elements  $i$  and  
 215  $j$ .



216 Deep infiltration and recharge fluxes are similarly calculated using the Richards  
217 equation as in the shallow zone:

$$218 \quad q_{infil}^{deep} = AK_{infil}^{deep} \frac{H_s^{shallow} - H_u^{deep}}{0.5 [H_s^{shallow} + (D^{deep} - H_s^{deep})]} \quad (9)$$

$$219 \quad q_{rechg}^{deep} = AK_{effV}^{deep} \frac{H_u^{deep} - H_s^{deep}}{0.5D^{deep}} \quad (10)$$

220 Where  $K_{infil}^{deep}$  is the hydraulic conductivity of infiltration from the shallow zone to the deep  
221 zone;  $D^{deep}$  is the thickness of the deep zone;  $K_{effV}^{deep}$  is the effective hydraulic conductivity  
222 in the vertical direction of the deep zone.

223 The deep groundwater can also come from regional groundwater aquifers, which  
224 can set up as an influx from the boundary of the domain. Deep groundwater interacts with  
225 river channel via the shallow zone. When the level of deep groundwater is higher than the  
226 depth to the deep zone, i.e., the shallow transient groundwater and the deep groundwater  
227 are connected, the deep groundwater can flow into the transient saturated layer in the  
228 shallow zone:

$$229 \quad q_{infil}^{deep} = -AK_{satV}^{deep} \quad (11)$$

230 Where  $K_{satV}^{deep}$  is the saturated hydraulic conductivity in the vertical direction of the deep  
231 zone.

232 **Macropores.** Macropores, including roots and soil cracks are omnipresent in soils.  
233 Macropore flows can be simulated in the model to account for rapid water flows in the  
234 shallow zone (Shi et al., 2013). Macropore properties include depth ( $D_{mac}$ ) and macropore  
235 vertical and horizontal area fraction ( $f_{macV}$  and  $f_{macH}$ ), and vertical and horizontal  
236 hydraulic conductivity ( $K_{macV}^{shallow}$  and  $K_{macH}^{shallow}$ ). The macropore depth differs from the  
237 rooting depth, which specifies the maximum depth of transpiration. By default  $K_{macV}^{shallow}$   
238 and  $K_{macH}^{shallow}$  are 100 and 1,000 times of the infiltration hydraulic conductivity ( $K_{infil}^{shallow}$ )  
239 and shallow horizontal hydraulic conductivity ( $K_{satH}^{shallow}$ ), respectively, and can be changed  
240 during calibration. Taking both soil and macropore properties into account, the effective



241 hydraulic conductivity of the subsurface is calculated as the weighted average of the  
242 macropore and the shallow soil matrix within the macropore depth (Eq. (12) and (13)).

$$243 \quad K_{effV}^{shallow} = f_{macH} K_{macV}^{shallow} + (1 - f_{macH}) K_{satV}^{shallow} \quad (12)$$

$$244 \quad K_{effH}^{shallow} = f_{macV} K_{macH}^{shallow} + (1 - f_{macV}) K_{satH}^{shallow} \quad (13)$$

245

### 246 **3.2 Biogeochemical reactive transport equations**

247 The governing equation for an arbitrary solute  $m$  in grid  $i$  is as follows (Bao et al.,  
248 2017):

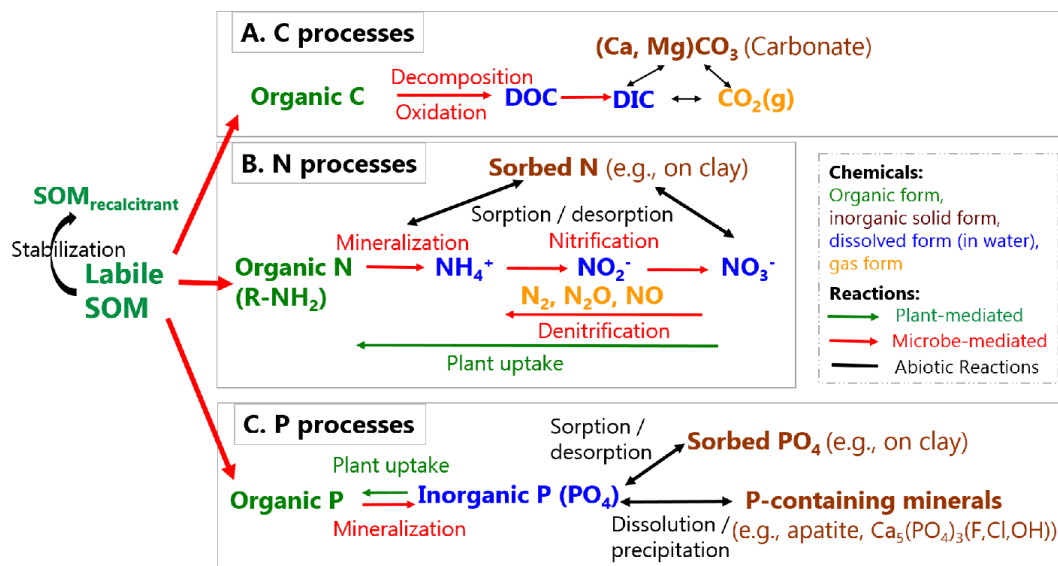
$$249 \quad V_i \frac{d(S_{w,i} \theta_i C_{m,i})}{dt} = \sum_{j=N_{i,1}}^{N_{i,x}} \left( A_{ij} D_{ij} \frac{C_{m,j} - C_{m,i}}{I_{ij}} - q_{ij} C_{m,j} \right) + R_{m,i} \quad (14)$$

250 Where  $V_i$  is the total volume of grid  $i$  (solid + liquid volume),  $m^3$ ;  $S_{w,i}$  is soil water  
251 saturation,  $m^3$  water/ $m^3$  pore space;  $\theta_i$  is porosity,  $m^3$  pore space/ $m^3$  total volume;  $C_{m,i}$  is  
252 the aqueous concentration of species  $m$ , mol/ $m^3$  water;  $N_{i,x}$  is the index of elements  
253 sharing surfaces; the value of  $x$  is 2 for the unsaturated zone (infiltration, recharge) and  
254 4 for the saturated zone (recharge plus three lateral flow directions), respectively;  $A_{ij}$  is  
255 the interface area ( $m^2$ ) shared by  $i$  and its neighbor grid  $j$ ;  $D_{ij}$  is the combined  
256 dispersion/diffusion coefficient ( $m^2/s$ ) normal to the shared surface  $A_{ij}$ ;  $I_{ij}$  is the distance  
257 between the center of  $i$  and its neighbor elements  $j$ ;  $q_{ij}$  is the flow rate across  $A_{ij}$ ,  $m^3/s$ ;  
258  $R_m$  is the total rate of kinetically controlled reactions that involve species  $m$ , mol/s.

259 Various types of reaction occur in the subsurface (Fatichi et al., 2019). Generally  
260 speaking, shallow soils contain more weathered materials and organic matters (OM)  
261 including roots, leaves, and microbe. In contrast, deeper zones are less weathered and contain  
262 much less organic matter. SOM can decompose partially into organic molecules that  
263 dissolve in water (Wieder et al., 2015), i.e., DOC, or oxidize completely into  $CO_2$  gas or  
264 dissolved inorganic carbon (DIC). With coexisting divalent cations (e.g., Ca, Mg), DIC can  
265 also precipitate and become carbonate minerals. Hence soil C decomposition can release  
266  $CO_2$  back into the atmosphere and changes  $CO_2$  level (Davidson, 2006), or releases DOC



267 and DOM to surface water. These processes occur in soils and also as dissolved carbon  
 268 transport laterally to streams.



269  
 270 **Figure 3.** Various types of biotic and abiotic reactions relevant to the transformation of soil organic  
 271 matter (SOM). It can become stabilized through sorption on clay and separation from reactants.  
 272 It can also decompose into inorganic forms, transitioning between different phases (adopted from  
 273 Li (2019), permission with Mineralogical Society of America).

274  
 275 Shown in Figure 3, SOM decomposition releases organic nitrogen (R-NH<sub>2</sub>), which  
 276 can further react to become ammonia, and other forms in between (N<sub>2</sub>, N<sub>2</sub>O, NO, N<sub>2</sub>O<sub>3</sub>  
 277 (NO<sub>2</sub><sup>-</sup>), NO<sub>2</sub>). Some of the gaseous forms emit back to the atmosphere (Saha et al.,  
 278 2017;Maavara et al., 2018). Denitrification requires anoxic conditions and does not occur  
 279 as much in shallow soils owing to the pervasive presence of O<sub>2</sub> (Sebestyen et al., 2019);  
 280 it can become prevalent however under extremely wet conditions and in O<sub>2</sub>-depleted  
 281 groundwater systems. In soils, P can be in organic form (e.g., leaves), sorbed (on fine  
 282 soil particles), dissolved in water, or in solid forms as P-containing minerals (Figure 3).  
 283 The transformation between different forms occurs through various bio-mediated or  
 284 abiotic reactions. The most abundant P-containing mineral is apatite Ca<sub>5</sub>(PO<sub>4</sub>)<sub>3</sub>(F, Cl,  
 285 OH). Once liberated via rock dissolution, P is mostly locked in organisms. It is barely  
 286 soluble so it binds on and transports together with soil particles in the form of



287 orthophosphate or pyro-diphosphate. Overall, these reactions are a combination of biotic  
288 and abiotic reactions.

289 BioRT can simulate biotic reactions including microbe-mediated reactions and plant  
290 uptake, in addition to the abiotic reactions such as mineral dissolution and surface complexation  
291 or ion exchange that have been introduced by Bao et al. (2017). Here we focus on the discussion  
292 of a few representative microbe-mediated reactions.

293

294 **Microbe-mediated reaction kinetics.** SOM is often conceptualized and modeled as  
295 pools with different decomposition rates and turnover times (Ostle et al., 2009; Thornton  
296 et al., 2009). An extensively used three-pool model includes a readily degradable (labile)  
297 pool with residence times less than five years; a slowly degrading pool with residence  
298 times of decades; and a relatively stable pool, with residence times between  $10^3 - 10^5$   
299 years (Trumbore et al., 1995; Trumbore, 1993; Marin-Spiotta et al., 2009). The kinetics of  
300 microbe-mediated reactions can be described by the general dual Monod rate law,  
301 reflecting the need for both electron donor and acceptor in these reactions (Monod, 1949):

302

$$r = \mu_{max} C_{C_5H_7O_2N} \frac{C_D}{K_{m,D} + C_D} \frac{C_A}{K_{m,A} + C_A} \quad (15)$$

303 Here  $\mu_{max}$  is the rate constant (mol/time/microbe cell),  $C_{C_5H_7O_2N}$  is the concentration of  
304 microorganisms (microbe cells/L<sup>3</sup>),  $C_D$  and  $C_A$  are the concentrations of electron donor  
305 and acceptor (mol/L<sup>3</sup>), respectively. The  $K_{m,D}$  and  $K_{m,A}$  are the half-saturation coefficients  
306 of the electron donor and acceptors (mol/m<sup>3</sup>), respectively; they are the concentrations at  
307 which half of the maximum rates are reached for the electron donor and acceptor,  
308 respectively. If an electron donor or acceptor is not limiting, it means that  $C_D \gg K_{m,D}$  or  
309  $C_A \gg K_{m,A}$ , so that the term  $\frac{C_D}{K_{m,D} + C_D}$  or  $\frac{C_A}{K_{m,A} + C_A}$  is essentially 1, leading to a rate that only  
310 depends on the abundance of microorganisms or one of the chemicals.

311 In natural subsurface where multiple electron acceptors coexist, the  
312 biogeochemical redox ladder dictates the sequence of redox reactions. That is, aerobic  
313 oxidation occurs before denitrification, which in turn occurs before iron reduction.  
314 Inhibition terms are used to account for the sequence of redox reactions as follows:



$$315 \quad r = \mu_{max} C_{C_5H_7O_2N} \frac{C_D}{K_{m,D} + C_D} \frac{C_A}{K_{m,A} + C_A} \frac{K_{I,H}}{K_{I,H} + C_H} \quad (16)$$

316 Here  $K_{I,H}$  is the inhibition coefficient for the inhibiting chemical  $H$ . The inhibition term is 1  
 317 (not inhibiting) only when  $C_H \ll K_{I,H}$ . In a system where oxygen and nitrate coexist, which  
 318 is common in agriculture lands, aerobic oxidation occurs first before denitrification. The  
 319 denitrification rates can be represented by:

$$320 \quad r_{NO_3^-} = \mu_{max} C_{C_5H_7O_2N} \frac{C_D}{K_{m,D} + C_D} \frac{C_{NO_3^-}}{K_{m,A} + C_{NO_3^-}} \frac{K_{I,O_2}}{K_{I,O_2} + C_{O_2}} \quad (17)$$

321 Here  $C_{NO_3^-}$  is the concentration of nitrate,  $K_{I,O_2}$  is the inhibition coefficient of  $O_2$ , or the  $O_2$   
 322 concentration at which it inhibits the reduction of nitrate. This rate law ensures that  
 323 denitrification kicks in substantially only when  $O_2$  is depleted to  $C_{O_2} \ll K_{I,O_2}$ , such that the  
 324 term  $\frac{K_{I,O_2}}{K_{I,O_2} + C_{O_2}}$  approaches 1.0. If there exists an electron acceptor that is lower in the  
 325 redox ladder than nitrate, multiple inhibition terms are needed. For example, for iron  
 326 oxide, we write the following:

$$327 \quad r_{Fe(OH)_3} = \mu_{max} C_{C_5H_7O_2N} \frac{C_D}{K_{m,D} + C_D} \frac{C_{Fe(OH)_3}}{K_{m,Fe(OH)_3} + C_{Fe(OH)_3}} \frac{K_{I,O_2}}{K_{I,O_2} + C_{O_2}} \frac{K_{I,NO_3^-}}{K_{I,NO_3^-} + C_{NO_3^-}} \quad (18)$$

328 Here  $K_{I,NO_3^-}$  is the  $NO_3^-$  concentration above which it inhibits iron reduction. The additional  
 329 nitrate inhibition term means that iron reduction occurs at significant rates only when both  
 330 oxygen and nitrate are low compared to their corresponding inhibition coefficients.

331

332 **Rates in natural soils.** The dual-Monod and inhibition terms are important under  
 333 conditions where electron donors and acceptors are limited. In shallow soil,  $O_2$  is  
 334 prevalent except under wet conditions with little pore space for air. Anoxic conditions can  
 335 also develop in local environments such as dead-end pores where water is saturated for  
 336 a long time and not easily flows out. Under conditions organic carbon and  $O_2$  are  
 337 abundant, the SOM rate law is simplified to the following form assuming microorganism  
 338 concentrations are relatively constant:

$$339 \quad r_{SOM} = \mu_{max} Af(T)f(S_w) \quad (19)$$



340 Where the reaction rate  $r_{SOM}$  (mol /t) now depends on  $\mu_{max}$  (mol/m<sup>2</sup>/t), the lumped  
341 surface area  $A$  (m<sup>2</sup>) as an approximation of SOM content and biomass abundance, and  
342  $f(T)$  and  $f(S_w)$  describe its temperature and soil moisture dependence, respectively. For  
343 temperature dependence, a Q<sub>10</sub>-based form (Friedlingstein et al., 2006;Hararuk et al.,  
344 2015) is commonly used:  $f(T) = Q_{10}^{|T-20|/10}$ , where  $Q_{10}$  is the relative increase in  
345 reaction rates when temperature increases by 10 °C (Davidson and Janssens, 2006). The  
346  $f(S_w)$  accounts for the nonlinear dependence of rates on soil moisture. A simple form  
347 of  $f(S_w) = (S_w)^\varepsilon$  where  $\varepsilon$  is the saturation exponent (a typical  $\varepsilon$  value is 2, with a range  
348 between 1.5 and 2.5) is often used. More complex forms of  $f(S_w)$  considering both water  
349 limitation under dry conditions and O<sub>2</sub> limitation under wet conditions have been proposed  
350 (Yan et al., 2018). It has also been suggested that the decomposition depends strongly  
351 on the depth distribution of SOM (Seibert et al., 2009), which is sometime accounted with  
352 an additional depth function:

$$353 \quad r_{SOM} = \mu_{max} A f(T) f(S_w) f(Z_w) \quad (20)$$

354 where  $Z_w$  is the water table depth (m). An example is  $f(Z_w) = \exp\left(-\frac{Z_w}{b_m}\right)$  (Weiler and  
355 McDonnell, 2006;Ottoy et al., 2016;Bai et al., 2016). Here  $b_m$  is the declining coefficient  
356 describing the gradient of SOM content over depth.

357

#### 358 4. Numerical scheme and model verification

359 **Numerical scheme.** The local system of differential equations for water storages [e.g.,  
360 Eq. (1), (2), (6), and (7)] on each control volume are combined into a global system of  
361 ordinary differential equations (ODEs) and solved in CVODE, a numerical ODE solver in  
362 the SUite of Nonlinear and Differential / ALgebraic equation Solvers (SUNDIALS)  
363 (Hindmarsh et al., 2005). CVODE is a numerically efficient solver for ODE systems. It  
364 uses the backward difference formula (BDF) with adaptive time steps and method order  
365 varying between 1 and 5. At each iteration step, the solver evaluates the local error, which  
366 is required to satisfy convergence tolerance conditions set by the users. The internal time  
367 step is reduced and the method order is adjusted in response to the stiffness of ODEs if  
368 the non-convergence occurred. For example, the solver time steps become smaller after



369 heavy precipitation events to address the rapid change of surface and subsurface water  
370 storages. The adaptive time stepping and order adjustment scheme make CVODE an  
371 accurate and stable solver.

372

373 **Model verification.** The BioRT module had been verified against CrunchTope under a  
374 variety of transport and reaction conditions at a range of reaction complexity levels  
375 (Supporting Information, Figure S1 – S7). CrunchTope is a widely used subsurface  
376 reactive transport model (Steefel and Lasaga, 1994; Steefel et al., 2015), and is often used  
377 as a benchmark to verify other reactive transport models. Verification is performed under  
378 simplified hydrological conditions with 1-D column and constant flow rates such that it  
379 focuses on biogeochemical reactive transport processes such as advection, diffusion,  
380 dispersion, and biogeochemical reactions. Specifically, three cases of soil phosphorus,  
381 carbon, and nitrogen were verified for temporal evolution and spatial pattern of relevant  
382 solute concentrations (Figure S1 – S7). The soil phosphorus case, which involves  
383 geochemically kinetic and thermodynamic processes (i.e., apatite dissolution and  
384 phosphorous speciation), was first tested for solution accuracy of the bulk code that was  
385 inherited from the original RT-Flux-PIHM. Soil carbon and nitrogen processes that involve  
386 microbially driven processes, such as soil carbon decomposition and mineralization,  
387 nitrification and denitrification, were further verified for solution accuracy of the  
388 augmented BioRT module.

389

## 390 **4 Model setup and data needs**

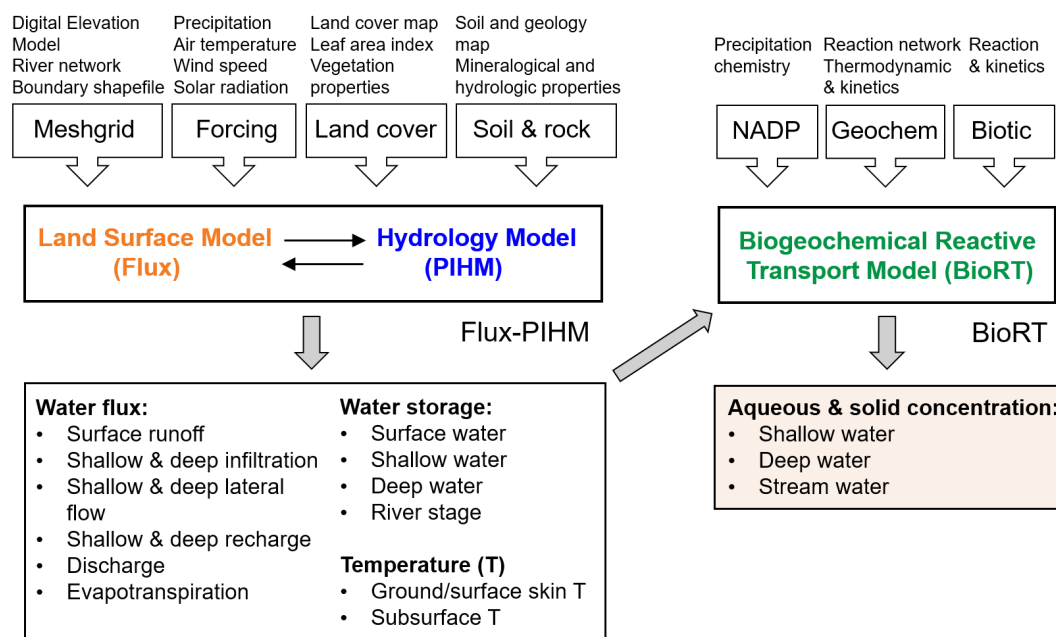
### 391 **4.1 Model structure and input/output**

392 Flux-PIHM sets up the domain based on watershed characteristics including  
393 topography, hydrography, land cover, and shallow and deep zone properties (Figure 4).  
394 It takes in meteorological forcing and solves for water storages and soil temperature.  
395 BioRT takes in the model output of water and temperature, and drives the simulation for  
396 biogeochemical reactive transport. At the time scale of months to years that are typical  
397 for BioRT-Flux-PIHM simulations, the alteration in solid phase properties due to reactions  
398 is considered negligible and does not change hydrological parameters.





399



400

401 **Figure 4.** Model structure, input, and output of BioRT-Flux-PIHM. The Flux-PIHM takes in  
 402 watershed characteristics including topography (digital elevation model, DEM), land cover,  
 403 shallow and deep zone properties, and meteorological forcing and then solves for water storage  
 404 and fluxes, and ground and soil temperature. Water- and temperature-related information from  
 405 Flux-PIHM with additional inputs such as precipitation chemistry and shallow and deep water  
 406 chemistry and biogeochemical kinetics parameters are then provided for the BioRT module, which  
 407 eventually outputs aqueous and solid concentration for the shallow and deep zone, and stream  
 408 water. NADP stands for the National Atmospheric Deposition Program.

409

410 Most model inputs such as elevation, land cover, soil and geology map can be  
 411 obtained from the data portal of Geospatial Data Gateway  
 412 (<https://datagateway.nrcs.usda.gov>). The meteorological forcing data can be downloaded  
 413 from the North American Land Data Assimilation Systems Phase 2 (NLDAS-2,  
 414 <https://ldas.gsfc.nasa.gov/nldas/v2/forcing>). The vegetation forcing, i.e., Leaf Area Index  
 415 (LAI), is from the Moderate Resolution Imaging Spectroradiometer  
 416 (<https://modis.gsfc.nasa.gov/data>). Other vegetation properties associated with land  
 417 cover (e.g., shading fraction, rooting depth) are adopted from the Noah vegetation  
 418 parameter table embedded in the Weather Research and Forecasting model (WRF;



419 Skamarock and Klemp (2019)). Local measurements from meteorological stations and  
420 field campaigns (e.g., land cover, soil, geology) can also be used in the model. Another  
421 data source for the model input is the HydroTerre (<http://www.hydroterre.psu.edu/>), where  
422 users can obtain geospatial data (Leonard and Duffy, 2013). The form of microbial  
423 reaction rate laws, when it includes full Monod form, or only with temperature and soil  
424 moisture dependence, can be defined in the input files. Additional inputs include initial  
425 water and solid phase chemistry, description of solutes and biogeochemical reactions,  
426 and kinetics and thermodynamics of reactions from a geochemical database. The model  
427 outputs include aqueous and solid concentrations of shallow and deep zone and stream  
428 water.

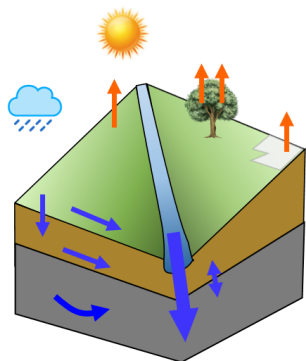
429

#### 430 **4.2 Model setup: from simple, spatially implicit to complex, spatially explicit** 431 **domains**

432 The model domain can be set up using PIHM-GIS  
433 ([http://www.pihm.psu.edu/pihmgis\\_home.html](http://www.pihm.psu.edu/pihmgis_home.html)), a standalone GIS interface for watershed  
434 delineation, domain decomposition, and parameter assignment (Bhatt et al., 2014). The  
435 domain can be set up at different spatial resolutions with a different number of grids. A  
436 simple domain can be set up with only two land grids representing two sides of a  
437 watershed connected by one river cell (Figure 5). This setup uses averaged properties  
438 without considering spatial details. This type of model setup requires less spatial data, is  
439 computationally inexpensive, and is relatively easy to set up. It can be used to assess the  
440 average dynamics of the water and solute dynamics and focus on the interactions among  
441 processes without concerning spatial details. It can also be used as a relatively easy  
442 starter for educational purposes before students jump into complex domains.  
443 Alternatively, a complex domain can be set up using many grids with explicit  
444 representation of spatial details. It requires much more data and is computationally  
445 expensive but can be used to identify “hot spots” of biogeochemical reactions.

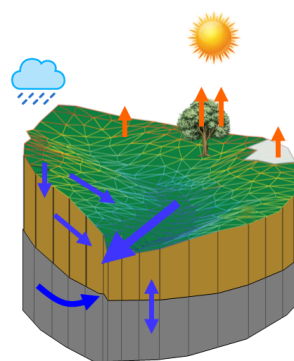


**Simple configuration:** spatially implicit mesh (2 land + 1 river cells)



Homogenized properties

**Complex configuration:** spatially explicit mesh (multiple land and river cells)



Heterogenized properties

Same model processes could be realized in both configurations:

- Land-surface process
- Hydrological process
- Biogeochemical process

446

447 **Figure 5.** Two extreme model domain setups: a simple domain with two land cells representing  
 448 two hillslopes connected by one river cell, versus a complex domain with hundreds of land cells.  
 449 An intermediate number of grids can also set up the domain, depending on watershed  
 450 heterogeneity, data availability, and desired spatial resolution.

451

## 452 5. Model applications

453 The original RT-Flux-PIHM has been applied to understand the processes related to  
 454 geogenic solutes of Cl and Mg at the Shale Hills watershed and for geogenic Na at the  
 455 Volcán Chimborazo watershed (Table 1). The new BioRT-Flux-PIHM has been  
 456 demonstrated for understanding the dynamics of DOC, nitrate, and Na at Shale Hills and  
 457 Coal Creek. This section presents some new model features using two examples: one  
 458 with a simple, spatially implicit domain, and another with a complex, spatially explicit  
 459 domain.

460

**Table 1.** Model applications with different biogeochemical reactions

Watershed (location)	Size (km <sup>2</sup> )	Model domain	Modeled solute	Reaction network (Kinetic rate law: 1, TST; 2, Monod based; 3, plant uptake rate)	Reference



		Complex (535 grids)	Cl, Mg	<ul style="list-style-type: none"> <li>• Chlorite dissolution<sup>1</sup></li> <li>• Illite dissolution<sup>1</sup></li> <li>• Carbonate dissolution &amp; precipitation<sup>1</sup></li> <li>• Cation exchange</li> </ul>	Bao et al., 2017; Li et al., 2017
Shale Hills (PA, USA)	0.08	Complex (535 grids)	DOC	<ul style="list-style-type: none"> <li>• SOC decomposition<sup>2</sup></li> <li>• DOC sorption</li> </ul>	Wen et al., 2020
		Simple (2 grids)	NO <sub>3</sub> <sup>-</sup>	<ul style="list-style-type: none"> <li>• Soil N leaching<sup>2</sup></li> <li>• Denitrification<sup>2</sup></li> <li>• Plant nitrate uptake<sup>3</sup></li> </ul>	This work
Coal Creek (CO, USA)	53	Simple (2 grids)	DOC, Na	<ul style="list-style-type: none"> <li>• SOC decomposition<sup>2</sup></li> <li>• DOC sorption</li> <li>• Albite dissolution<sup>1</sup></li> </ul>	Zhi et al., 2019
Volcán Chimborazo (Ecuador)		Complex (160 grids)	Cl, Na, Ca, Mg, SiO <sub>2</sub>	<ul style="list-style-type: none"> <li>• Albite dissolution<sup>1</sup></li> <li>• Diopside dissolution<sup>1</sup></li> </ul>	Leila et al., 2020 (under review)

461 Note: Transition State Theory (TST) is a classic kinetic rate law for mineral dissolution and  
 462 precipitation (Brantley et al., 2008); Monod based rate law with environmental dependency (i.e.,  
 463 soil temperature and soil moisture) is widely used for microbial driven reactions; plant nitrate  
 464 uptake depends on nitrate availability, environmental dependency, and rooting depth. Monod  
 465 based and plant nitrate uptake rate law are detailed in the following section of 5.1.1.

466

467 Here we present two examples of different processes in the Susquehanna Shale  
 468 Hills Critical Zone Observatory (SSHCZO), a small headwater watershed (0.08 km<sup>2</sup>) in  
 469 central Pennsylvania, USA. The mean annual precipitation is approximately 1,070 mm  
 470 and the mean annual temperature is 10 °C. Extensive field measurements have been  
 471 conducted to characterize the topography, vegetation, and bedrock and soil properties  
 472 (Brantley et al., 2018). Soil carbon storage and respiration and nitrogen budget and fluxes  
 473 have been detailed studied (Andrews et al., 2011; Hasenmueller et al., 2015; Shi et al.,  
 474 2018; Hodges et al., 2019; Weitzman and Kaye, 2018). Modeling work has also been  
 475 conducted to understand hydrological dynamics (Shi et al., 2013), transport of a non-  
 476 reactive tracer Cl and the soil and rock weathering Cl and Mg (Bao et al., 2017; Li et al.,  
 477 2017a).



478

## 479 **5.1 Hydrology Example: Shallow and deep water interactions**

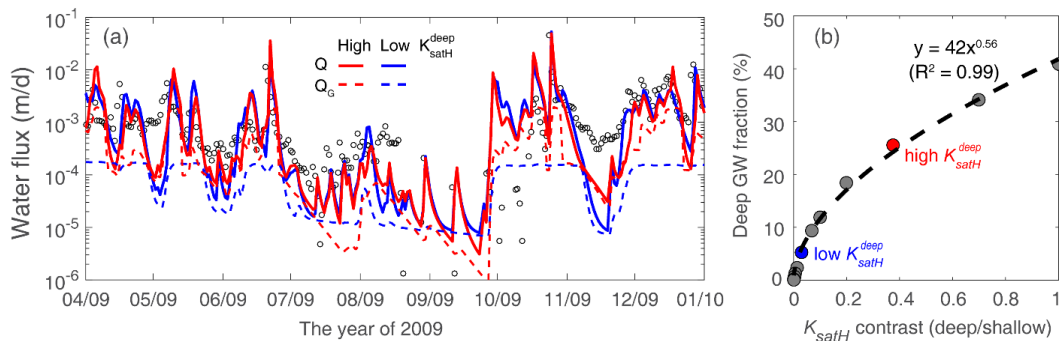
480 The model was set up using two land grids and one river grid, represented by the  
481 averaged land cover, soil and rock properties based on previous work (Shi et al.,  
482 2013;Kuntz et al., 2011). Specifically, the model assumed a Weikert soil, the dominant  
483 soil type at Shale Hills (Shi et al., 2013). The porosity of the deep zone was set to 1/10 of  
484 the shallow soil porosity based on measurements of the deep subsurface (Brantley et al.,  
485 2018;Kuntz et al., 2011). Stream discharge and ET observations were used to calibrate  
486 hydrological parameters (Figure S9). Groundwater ( $Q_G$ ) from the deep layer was  
487 constrained by previous work (Li et al., 2017a) and the nitrate concentration-discharge  
488 (C-Q) observations. Important land surface and hydrological parameters are summarized  
489 in Table S7.

490 **Water budget.** The model reproduced the seasonal dynamics of discharge and ET  
491 (Figure S9), with daily Nash-Sutcliffe efficiency (NSE) of 0.56 and 0.66, respectively.  
492 Precipitation occurs throughout the year while the discharge was responsive to a few big  
493 storm events in spring and fall. The ET peaked during the summer due to higher solar  
494 radiation and higher temperature while declined in the fall and winter. The runoff ratio was  
495 0.46, suggesting 46% of precipitation was discharged through the stream while the  
496 remaining 54% contributed to ET. A breakdown analysis suggests at the annual scale,  
497 the shallow lateral flow ( $Q_L$ , 87% of  $Q$ ) dominated discharge, followed by the deeper  
498 groundwater flow ( $Q_G$ , 9.3%), and the surface runoff ( $Q_S$ , 4.2%). The  $Q_G$  was essential in  
499 maintaining discharge during dry time, especially in the summer.

500 **Controls of deep water.** In a headwater watershed like Shale Hills where the deep  
501 groundwater is most likely sourced from recharge, the deep groundwater contribution to  
502 the stream was primarily controlled by hydraulic conductivity ( $K_{satH}$ ) contrast between the  
503 deep and shallow zone (i.e.,  $K_{satH}^{deep} / K_{satH}^{shallow}$ ). Because the  $K_{satH}$  contrast determined the  
504 partitioning of infiltrating water between the shallow lateral flow and the downward  
505 recharge to the deep zone and then deep groundwater flow. Two cases of high (red) and  
506 low (blue)  $K_{satH}^{deep}$  were set up to showcase the  $K_{satH}$  contrast control on deep groundwater



507 (Figure 6a). By changing the deep zone  $K_{satH}^{deep}$  from 2.6 to 0.22 (m/d), about 38% and 3.1%  
508 of the shallow zone  $K_{satH}^{shallow}$ , annual deep groundwater ( $Q_G$ ) contribution to discharge ( $Q$ )  
509 decreased from 26% to 5.2%, respectively. It is also noticeable that there was minimal  
510 change between discharge (i.e., solid lines in Figure 6a) as the deep zone  $K_{satH}^{deep}$  does not  
511 affect shallow water partitioning for infiltrating water and discharge. This new hydrology  
512 feature enables the exploration of the interaction between deep groundwater and surface  
513 water. These features can be used to understand watersheds of different subsurface  
514 structures and with deep water mostly from recharge. In addition, they can be used to  
515 explore large watersheds of higher stream order with a large proportion of deep water  
516 coming from nearby regional aquifers.



517  
518 **Figure 6.** (a) Hydraulic conductivity ( $K_{satH}$ ) contrast control on deep groundwater ( $Q_G$ ).  
519 The cases of high (red) and low (blue)  $K_{satH}^{deep}$  led to 26% and 5.2% of annual  $Q_G$   
520 contribution to discharge ( $Q$ ), respectively. (b) Deep groundwater fraction as a function of  
521  $K_{satH}$  contrast between the deep and shallow zone. The  $K_{satH}$  contrast was limited to 1  
522 in the figure as most watersheds exhibit a smaller  $K_{satH}$  in the deep zone than in the  
523 shallow zone. The two red and blue dots correspond to the two cases in left panel.

524  
525 A series of similar cases were further tested to generate the relationship between  
526 deep groundwater fraction (%) of discharge and  $K_{satH}$  contrast (Figure 6b). Results show  
527 that the deep groundwater fraction exponentially increased with the increasing  $K_{satH}$   
528 contrast, reaching a limit at when  $K_{satH}$  contrast is sufficiently high. The results also  
529 suggest that the maximum deep groundwater contribution to the stream was limited to ~  
530 40% as most watersheds exhibit smaller  $K_{satH}^{deep}$  than  $K_{satH}^{shallow}$ . The fitting function (dashed

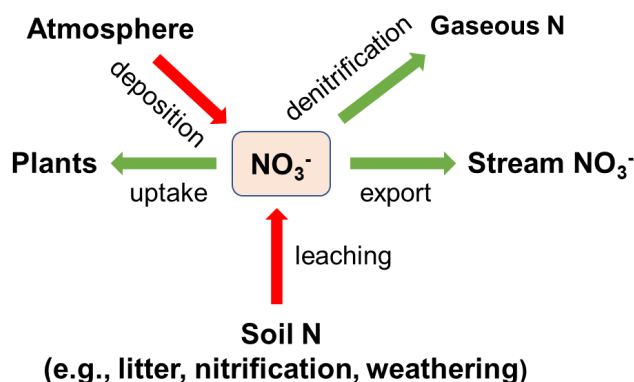


531 line) could be a useful predictor to quantify deep groundwater contribution at headwater  
532 watersheds given measured deep and shallow hydraulic conductivity.

533

## 534 **5.2 Reactive Transport Example 1: Understanding nitrate dynamics using a** 535 **spatially implicit domain**

536 This example focuses on nitrate, which is the dominant N form in water and has relatively  
537 abundant measurements from 2008 to 2010 ([https://criticalzone.org/shale-](https://criticalzone.org/shale-hills/data/datasets/)  
538 [hills/data/datasets/](https://criticalzone.org/shale-hills/data/datasets/)) (Weitzman and Kaye, 2018). Based on their field measurements, the  
539 atmospheric deposition was the dominant N input and export via discharge was only a  
540 small fraction (2.5%) of atmospheric N input. Most deposited N was either lost to the  
541 atmosphere via denitrification or uptaken by trees. The model at Shale Hills watershed  
542 included atmospheric N deposition, soil N leaching, stream export, denitrification, and  
543 plant uptake (Figure 7).



544

545 **Figure 7.** Modeled nitrogen processes at Shale Hills. Atmospheric N deposition was the major N  
546 sources (top red arrows); denitrification and plant uptake were the major N loss and sink (green  
547 arrows). Export from discharge removes nitrate but it was a relatively small one.

548

549 The soil N leaching process was a lumped reaction that generates  $\text{NO}_3^-$  source,  
550 including the decomposition of soil organic matter (SOM), nitrification, and rock  
551 weathering. Its rate was assumed to depend on soil temperature and moisture:

552

$$r_{leach} = kAf(T)f(S_w) \quad (21)$$



553 Here  $r_{leach}$  is the leaching rate (mol/s),  $k$  is the rate constant (mol/m<sup>2</sup>/s), and the surface  
554 area  $A$  (m<sup>2</sup>) is a lumped parameter representing the effective contact area between  
555 substrates and N transforming microbe. It was calculated based on SOM volume fraction  
556 (m<sup>3</sup>/m<sup>3</sup>), specific surface area (SSA, m<sup>2</sup>/g), substrate density (g/cm<sup>3</sup>), and element  
557 volume (m<sup>3</sup>).

558 The denitrification process converts NO<sub>3</sub><sup>-</sup> to N<sub>2</sub> gas under anaerobic conditions.  
559 This process can be modeled by the Monod rate law with nitrate as the electron acceptor  
560 substrate ( $K_{m,NO_3^-} = 45 \mu M$  (Regnier and Steefel, 1999; Billen, 1977)) and with inhibition  
561 from O<sub>2</sub> (Eq. (22)). Under conditions where O<sub>2</sub> concentration is not explicitly modeled (this  
562 work), the O<sub>2</sub> inhibitory term can be replaced by a function of soil moisture (Eq. (24)). This  
563 is based on field evidence that denitrification typically occurs when soil moisture is greater  
564 than 0.6 and increases with increasing soil moisture (Brady et al., 2008). Equation (24)  
565 says that under relatively drier conditions ( $S_w < 0.6$ ), there is sufficient O<sub>2</sub> that  
566 denitrification does not occur; under wet conditions ( $S_w \geq 0.6$ ), the O<sub>2</sub> becomes limiting  
567 such that denitrification can occur.

568 
$$r_{denitrification} = kA \left( \frac{C_{NO_3^-}}{K_{m,NO_3^-} + C_{NO_3^-}} \right) f(O_2) f(T) f(S_w) \quad (22)$$

569 
$$f(O_2) = \frac{K_{I,O_2}}{K_{I,O_2} + C_{O_2}} \quad (23), \text{ when } O_2 \text{ is explicitly modelled}$$

570 
$$f(O_2) = \begin{cases} 0 & (S_w < 0.6) \\ (S_w - 0.6) * 2.5 & (S_w \geq 0.6) \end{cases} \quad (24), \text{ when } O_2 \text{ is not explicitly modelled}$$

571

572 Nitrate uptake by plants is intrinsically complex and not yet completely understood  
573 (Devienne-Barret et al., 2000; Crawford and Glass, 1998; Hachiya and Sakakibara, 2016).  
574 A variety of plant uptake models exists in literature with varying levels of complexity  
575 (Neitsch et al., 2011; Fisher et al., 2010; Cai et al., 2016). These models are mostly based  
576 on plant growth module or supply and demand approach that often requires detailed  
577 phenological and plant attributes such as growth cycle, root age and biomass, nitrate  
578 availability, phosphorous stress, and carbon allocation, in addition to local climate  
579 conditions such as temperature and soil moisture (Neitsch et al., 2011; Porporato et al.,





580 2003;Dunbabin et al., 2002;Buysse et al., 1996;Fisher et al., 2010). Without all the  
581 detailed information, here we assumed a simple and operational approach to model  
582 nitrate uptake with dependence on  $\text{NO}_3^-$  concentration, soil temperature and moisture,  
583 and rooting density (Eq. (25), (26)). More detailed, user-tailored plant uptake rate law can  
584 be added if needed.

$$585 \quad r_{\text{uptake}} = k_{\text{uptake}} C_{\text{NO}_3^-} f(T) f(S_w) f_{\text{root}}(d_w) \quad (25)$$

$$586 \quad f_{\text{root}}(d_w) = \exp((-d_w + r) / s) \quad (26)$$

587 Where  $k_{\text{uptake}}$  is the nitrate uptake rate (L/s),  $f_{\text{root}}(d_w)$  is a normalized rooting density  
588 term in the range of 0 to 1 as a function of water depth to the groundwater ( $d_w$ ). The  
589 rooting term (Eq. (26)) was exponentially fitted ( $r = 0.0132, s = 0.202$ ) based on field  
590 measurements of root distribution along depth (Figure S8) (Hasenmueller et al., 2017).  
591 The exponentially declining root function is generally to be the case in forested  
592 watersheds but can be tailored to agricultural watersheds when field data are available.

593 For microbial soil N leaching and denitrification, reaction rate constant  $k$  was  
594 specified (Regnier and Steefel, 1999) and the lumped surface area  $A$  ( $\text{m}^2$ , = specific  
595 surface area  $\text{m}^2/\text{g} \times \text{g}$  of mass) was turned to reproduce stream nitrate dynamics and its  
596 C-Q pattern (Table S8). The calibrated effective specific surface area (SSA) were orders  
597 of magnitude lower than the lab measured SSA of natural materials (e.g., SOM, 0.6 ~ 2  
598  $\text{m}^2/\text{g}$ ) (Rutherford et al., 1992;Chiou et al., 1990). Such discrepancies between calibrated  
599 effective reactive surface area (i.e., solid-water contact area) and lab measured absolute  
600 surface area are consistent with other observations (Li et al., 2014;Heidari et al., 2017).  
601 The nitrate uptake rate constant  $k_{\text{uptake}}$  was calibrated to constrain the partitioning of N  
602 transformation flux between denitrification and plant uptake by the ratio of 1:5, a value  
603 estimated from field measurements of gaseous N outputs (3.53 kg-N/ha/yr) and plant N  
604 uptake (18.3 kg-N/ha/yr) (Weitzman and Kaye, 2018). We assumed that the nitrate uptake  
605 rate  $k_{\text{uptake}}$  of the deep zone ( $> 2$  m in depth) was 1/1000 of that in the shallow zone,  
606 based on the observations that the rooting density exponentially decrease with depth  
607 (Weitzman and Kaye, 2018;Hasenmueller et al., 2017). Groundwater nitrate was



608 initialized as 0.43 mg/L, the average of measured groundwater concentration during  
609 2009-2010.

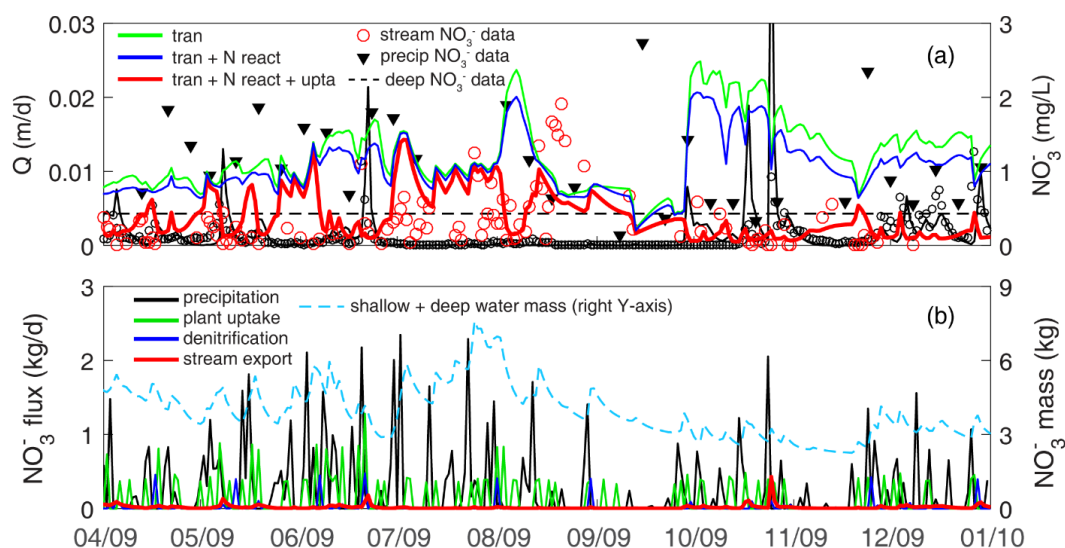
610 **Temporal dynamics.** Three cases were set up to understand and quantify the effects of  
611 different processes in determining the nitrate dynamics (Figure 8). The *transport-only*  
612 case (green line, *tran*) only has N input from precipitation (at  $1.4 \pm 0.96$  mg/L, based on  
613 the 2009 data of NADP PA42 site) and transport without any reactions. It overestimated  
614 stream nitrate data ( $0.33 \pm 0.39$  mg/L) throughout the year. The *transport + N reactions*  
615 case (blue line, *tran + N react*) has the denitrification and soil N leaching processes but  
616 not plant uptake. It lowered the nitrate concentration, suggesting their relative minor role  
617 in controlling N. The *transport + N reactions + uptake* case (red line, *tran + N react + upta*)  
618 have all processes. It significantly lowered the nitrate concentration, especially in April-  
619 May and October-December. There were some overestimated short nitrate peaks from  
620 May to July, exhibiting comparable levels of high precipitation nitrate concentration  
621 (Figure 8a). It is noticeable that the three cases (i.e., *transport-only*, *transport + N*  
622 *reactions*, *transport + N reactions + uptake*) almost overlapped (i.e., minimal difference)  
623 at these overestimated short nitrate peaks, suggesting the nitrate-rich precipitation was  
624 not routed into the subsurface where denitrification and plant uptake could occur and  
625 lower the nitrate concentration. In short, hydrology controlled stream nitrate dynamics by  
626 partitioning the nitrate-rich precipitation into surface runoff, shallow lateral flow, and deep  
627 groundwater. Nitrate reactions primarily controlled stream concentration via the  
628 subsurface flow flowpath where the nitrate-rich precipitation undergone significant nitrate  
629 loss and sink, as denitrification and plant uptake only occurred to remove nitrate in the  
630 subsurface but not in surface water.

631 Comparing the three outfluxes (Figure 8b), nitrate export via discharge (red) was  
632 negligible compared to denitrification (blue) and plant uptake (green). At the annual scale,  
633 stream nitrate export only accounted for 9.5% outfluxes, whereas denitrification and plant  
634 uptake took up 15% and 75% of precipitated  $\text{NO}_3^-$ , respectively. At Shale Hills, rock N  
635 leaching (weathering) is calculated up to 10% of N precipitation.

636 Although precipitation source occurred primarily from April to August (70% of total  
637 simulation period), larger storm events in October contributed more to the export. Deeper



638 groundwater had higher nitrate concentration than shallow water, because most plant  
639 uptake occurred in the shallow zone. The nitrate fluxes into the deeper zone however  
640 only contributed 26% of stream nitrate export at the annual scale, due to the relatively  
641 small groundwater contribution (9.5%) to the stream. Denitrification and plant uptake  
642 largely occurred during the wet period, which coincided with the growing season.  
643 Denitrification peaks often showed up after major storm events.



644

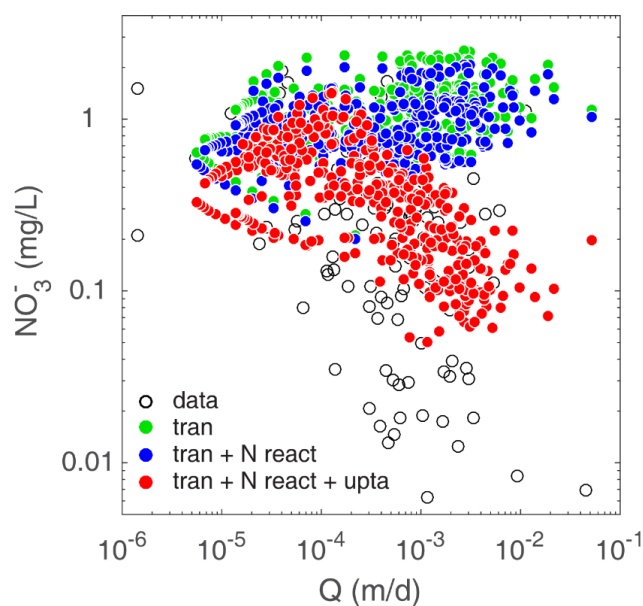
645 **Figure 8.** Stream nitrate dynamics at Shale Hills in three simulation conditions: *transport-only*  
646 (green line, *tran*), *transport + N reaction* (blue line, *tran + N react*), *transport + N reaction + plant*  
647 *uptake* (red line, *tran + N react + upta*), where N reactions include both nitrate leaching and  
648 denitrifications (see Figure 8). (a) stream nitrate dynamics; (b) nitrate fluxes and budget. Note the  
649 nitrate leaching was ignored in (b) due to its minimal flux as precipitation N deposition was as the  
650 dominant input source (Weitzman and Kaye, 2018).

651

652 **C-Q patterns.** C-Q plots from the three cases showed distinct patterns (Figure 9).  
653 Specifically, the *transport-only* (green) and *transport + N reactions* (blue) cases led to  
654 chemostatic or slightly flushing patterns while the *transport + N reactions + plant uptake*  
655 (red) case showed a dilution pattern similar to field observation. The *transport-only* case  
656 showed a slightly flushing pattern because the shallow water had slightly higher nitrate  
657 concentration (directly from precipitation without reactions) than deep groundwater. This  
658 results in low stream concentrations from deep groundwater at low flow conditions and



659 high stream concentrations from shallow water with higher nitrate at high flow conditions.  
660 With limited denitrification capacity (Figure 8a), the *transport + N reactions* case was  
661 similar to the *transport-only* case. In comparison, the plant uptake reduced nitrate  
662 concentration in the shallow zone, to an extent lower than the concentration in the deeper  
663 zone, altering the C-Q pattern from primarily chemostatic to dilution (Figure 9).



664  
665 **Figure 9.** Concentration-discharge (C-Q) relationships under three scenarios that involve different  
666 processes: *transport-only* (green, *tran*), *transport + N reactions* (blue, *tran + N react*), *transport +*  
667 *N reactions + plant uptake* (red, *tran + N react + upta*).

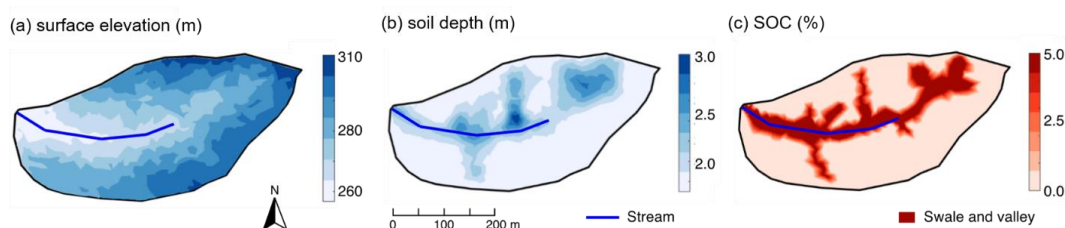
668  
669 **5.3 Reactive Transport Example 2: DOC production and export in a spatially explicit**  
670 **domain**

671 This example showcases the application of BioRT-Flux-PIHM in a spatially explicit  
672 mode. This work has been documented with full details in Wen et al. (2020). Here we only  
673 introduce some key features and capabilities in the spatially explicit mode.

674 **Model set-up.** In this example, the Shale Hills catchment was discretized into 535  
675 prismatic land elements and 20 stream segments through PIHMgis based on the  
676 topography (Figure 10a). The heterogeneous distributions of soil depth and solid organic



677 carbon within the domain (Figure 10b-c) were interpolated through ordinary kriging based  
678 on field surveys (Andrews et al., 2011;Lin, 2006). Other soil and mineralogy properties  
679 such as hydraulic conductivity, van Genuchten parameters, and ion exchange capacity  
680 were also spatially distributed following intensive field measurements across the  
681 catchment (Jin and Brantley, 2011;Jin et al., 2010;Shi et al., 2013) (criticalzone.org/shale-  
682 hills/data/).



683

684 **Figure 10.** Attributes of Shale Hills in the spatially explicit mode: (a) surface elevation, (b) soil  
685 depth, and (c) soil organic carbon (SOC). The surface elevation was generated from lidar  
686 topographic data (criticalzone.org/shale-hills/data); Soil depths and SOC were interpolated using  
687 ordinary kriging based on field surveys (Andrews et al., 2011;Lin, 2006). The SOC distribution in  
688 (c) was further simplified using the high, uniform SOC (5% v/v) in swales and valley soils based  
689 on field survey (Andrews et al., 2011). Swales and valley floor areas were defined based on  
690 surface elevation via field survey and a 10 m resolution digital elevation model (Lin, 2006).

691

692 DOC was produced by the decomposition of soil organic carbon (SOC) via the  
693 following reaction:



695 The produced DOC can sorb on soils via the sorption reaction:



697 where  $\equiv X$  and  $\equiv XDOC$  represent the functional group without and with sorbed DOC,  
698 respectively (Rasmussen et al., 2018). For DOC production, with abundant SOC and  $O_2$   
699 in shallow soils serving as electron donors and acceptors, Eq. (27) can be simplified into  
700  $r_{DOC} = kAf(T)f(S_w)$ , where  $r_{DOC}$  is the local DOC production rate in individual grids;  $k$  is  
701 the kinetic rate constant of net DOC production with a value of  $10^{-10}$  mol/m<sup>2</sup>/s (Zhi et al.,  
702 2019;Wieder et al., 2014); and  $A$  is the lumped “surface area” (m<sup>2</sup>, =  $2.5 \times 10^{-3}$  m<sup>2</sup>/g × g of  
703 SOC mass) that reflects the effective contact of water with SOC content and biomass



704 (Chiou et al., 1990; Kaiser and Guggenberger, 2003; Zhi et al., 2019). The temperature  
705 dependence function took the form  $f(T) = 2.0^{|T-20|/10}$  while the moisture dependence  
706 function followed  $f(S_w) = (S_w)^{1.0}$  (Yan et al., 2018; Hamamoto et al., 2010). In DOC  
707 sorption, equilibrium constant  $K_{eq}$  with a value of  $10^{0.2} (= \frac{[\equiv XDOC]}{[\equiv X][DOC]})$  represents the  
708 thermodynamic limit of the sorption; The sum of  $[\equiv X]$  and  $[\equiv XDOC]$  represents the  
709 sorption capacity of the soil with a value ranging from  $4.0 \times 10^{-5}$  -  $6.0 \times 10^{-5}$  mol/g soil at  
710 Shale Hills (Jin et al., 2010; Li et al., 2017a), depending on the mineralogy.

711

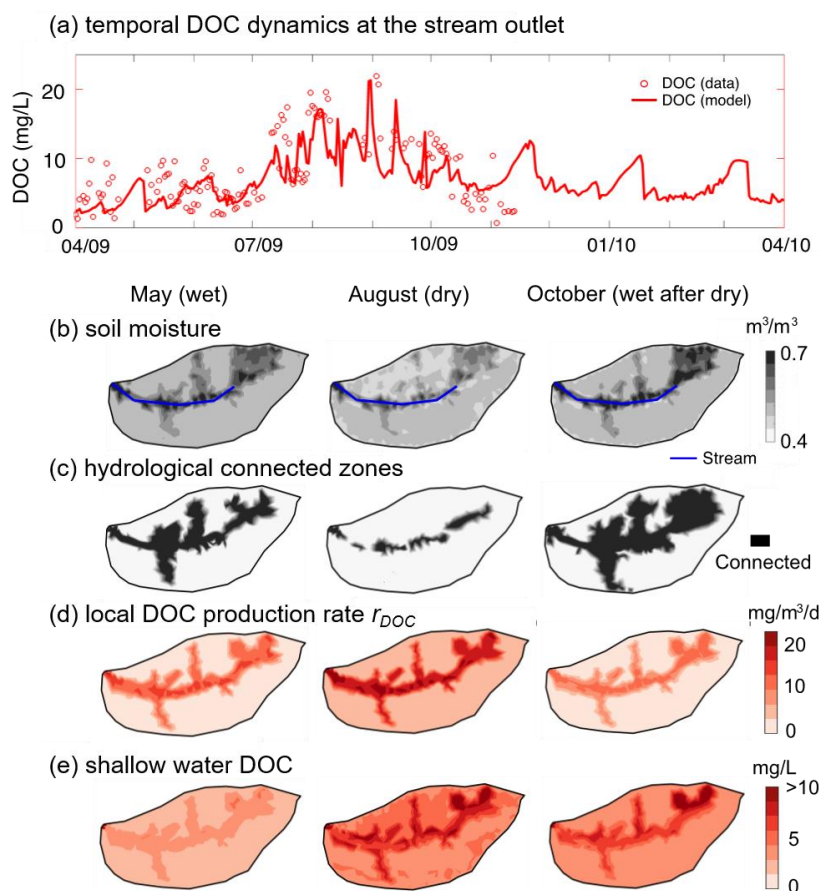
712 **Temporal and spatial patterns of DOC production and export.** The model outputs  
713 followed the general trend of stream DOC data (NSE = 0.55 for monthly DOC  
714 concentration; Figure 11a), with high values (~ 15 mg/L) in the dry periods (July-  
715 September). The model enabled the identification of spatial patterns and the hot spots of  
716 reactions. In May when soil water is relatively abundant, valley and swales with deeper  
717 soils (Figure 11b) generally tended to be wetter compared to the hillslope and ridgetop,  
718 and were hydrologically connected to the stream (Figure 11b-c). The distribution of local  
719 DOC production rate  $r_{DOC}$  and DOC concentration followed that of SOC (Figure 11c) and  
720 water content (Figure 11b). Low  $r_{DOC}$  in relatively dry planar hillslopes and uplands  
721 resulted in low soil water DOC. The average stream DOC (~ 5 mg/L) reflected soil water  
722 DOC in the valley and swales.

723 In August, the hydrologically-connected zones with high water content shrank to  
724 the vicinity of the stream and river bed. With high temperature in summer,  $r_{DOC}$  increased  
725 by 2-fold from May across the whole catchment while still exhibited the highest values in  
726 the SOC-rich regions. Soil water DOC concentration increased by a factor of 2 because  
727 the produced DOC was trapped in low soil moisture areas that were not hydrologically  
728 connected to the stream. In the north side with low water content (Figure 11b), the soil  
729 water DOC (~ 7 mg/L in average) accumulated more than the south side (~ 5 mg/L in  
730 average). The high shallow water DOC (~ 10 mg/L) in the stream vicinity dominated the  
731 stream DOC in August.

732 In October, precipitation wetted the catchment again. The hydrologically  
733 connected zones expanded beyond swales and valley to the upland hillslopes (Figure



734 11c). The increase in hydrological connectivity zones favored the mixture of shallow water  
735 DOC sourced from upland hillslopes (low DOC), swales, and valley (high DOC) into  
736 stream rather than only from the stream vicinity with high DOC in the dry August, leading to  
737 a drop in stream DOC.



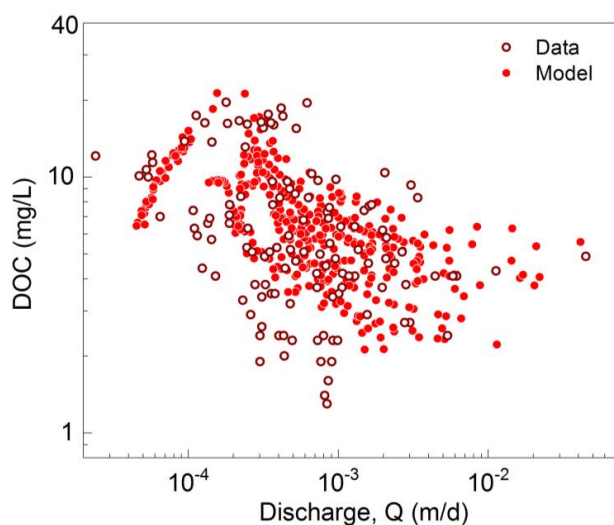
738

739 **Figure 11.** (a) Temporal dynamics of stream DOC concentration; spatial profiles of (b) shallow  
740 soil moisture, (c) hydrologically connected zones, (d) local DOC production rates  $r_{DOC}$  and (e)  
741 shallow water DOC concentration in May (wet), August (dry), and October (wet after dry) of 2009.  
742 The soil DOC and  $r_{DOC}$  were high in swales and valley with relatively high shallow water and SOC  
743 content. August had the highest shallow water DOC concentration compared to May and October,  
744 because most DOC accumulated in zones that are disconnected to the stream.

745



746 **C-Q patterns.** The DOC C-Q relationship showed a non-typical pattern with flushing first  
747 and transitioning into a dilution pattern, with a general (overall) C-Q slope  $b = -0.23$   
748 (Figure 12). At low discharges ( $< 1.8 \times 10^{-4}$  m/d) in summer dry period, the stream DOC  
749 mainly came from the organic-rich swales and valley floor zones with high soil water DOC  
750 (Figure 11e). With discharge increasing in wetter period (i.e., spring and fall), the  
751 contribution from planar hillslopes and uplands with lower DOC concentration increased  
752 (Figure 11e), leading to the dilution of stream DOC.



753

754 **Figure 12.** Relationships of daily discharge ( $Q$ ) with stream DOC concentration. With the increase  
755 of  $Q$ , the stream water first shifted from the dominance of groundwater with low DOC at very low  
756 discharge to the predominance of organic-rich soil water from swales and valley at intermediate  
757 discharge. As the discharge increases further, the stream water switches to the dominance of  
758 high flow with lower DOC water from planar hillslopes and uplands, resulting in a dilution C-Q  
759 pattern (modified from Wen et al., (2020)).

760

761 Compared to the spatially implicit model, the spatial representation enables the  
762 exploration on the “hot spots” (i.e., swales and riparian zones with high soil water DOC  
763 concentrations in Figure 11e) and their contribution to stream chemistry at different times.  
764 Spatial heterogeneities in watershed properties (e.g., soil types and depth, lithology,  
765 vegetation, biomass, and mineralogy) are omnipresent in natural systems. Yet a general  
766 understanding of the linkage between local catchment features and catchment-scale





767 dynamics (e.g., stream concentration dynamics and solute export pattern) is still lacking.  
768 Questions such as how the heterogeneous features affect water flow paths, stream water  
769 chemistry, and biogeochemical reaction rates remain largely unanswered. The spatially  
770 explicit model provides a tool to further explore these questions.

771

## 772 **6. Summary and conclusion**

773 This paper introduces the watershed-scale biogeochemical reactive transport code  
774 BioRT-Flux-PIHM. This code integrates processes of land-surface interactions, surface  
775 hydrology, and multi-component reactive transport. The new development enables the  
776 simulation of 1) biotic reactions including microbe-mediated redox reactions and plant  
777 uptake, and 2) surface water interactions with water from deeper subsurface zones.  
778 BioRT has been verified against the widely used reactive transport code CrunchTope for  
779 soil carbon, nitrogen, and phosphorus processes. The BioRT module has been applied  
780 to understand carbon, nitrogen, and weathering processes in Shale Hills in central  
781 Pennsylvania, Coal Creek in Colorado, and Volcán Chimborazo watershed in Andes in  
782 Ecuador. Here we showcase the modeling capability of surface-groundwater interactions,  
783 transport and reactive transport processes relevant to nitrate and DOC in Shale Hills in  
784 two simulation modes. One is in spatially implicit mode using averaged properties and  
785 another in spatially explicit mode with consideration of spatial heterogeneity. Results  
786 show that the deep groundwater that interacts with stream is primarily controlled by the  
787 hydraulic conductivity contrast between shallow and deep zone. Soil biogeochemical  
788 reactions in shallow soil primarily determines the shallow water chemistry, especially C,  
789 N, and biogenic solutes, under high flow conditions. The spatially implicit method with two  
790 grids can capture the temporal dynamics of average behavior and mass balance; the  
791 spatially explicit running mode can be used to understand the spatial dynamics and to  
792 identify 'hot spots' of reactions.

793

794 **Data availability.** Field data (e.g., discharge, stream chemistry) is archived at Shale Hills  
795 data portal: <http://criticalzone.org/shale-hills/data/datasets/> or maintained at HydroShare:  
796 <https://www.hydroshare.org/group/147>.

797



798 **Code availability.** The current model release (BioRT-Flux-PIHM v1.0), including  
799 documentation, source code, example data, is available at GitHub repository:  
800 <https://github.com/PSUmodeling/BioRT-Flux-PIHM>.

801

802 **Competing interests.** The authors declare that they have no conflict of interest.

803

804 **Author contributions.** LL conceived the model idea and oversaw the model  
805 development. WZ coded the BioRT module, verified the code against the benchmark  
806 reactive transport model CrunchTope, and applied and tested the model at Shale Hills  
807 watershed. YS developed the deep groundwater component and integrated the BioRT-  
808 Flux-PIHM v1.0 into MM-PIHM family. WH, LS, and GCHN tested the code during its  
809 development and contributed their study cases.

810

811 **Acknowledgement.** We acknowledge the funding support from the Department of  
812 Energy, Subsurface Biogeochemistry Program DE-SC0020146, National Science  
813 Foundation Hydrological Sciences EAR-1758795. We appreciate data from the  
814 Susquehanna Shale Hills Critical Zone Observatory (SSHCZO) supported by National  
815 Science Foundation Grant EAR – 0725019 (C. Duffy), EAR – 1239285 (S. Brantley), and  
816 EAR – 1331726 (S. Brantley). Data were collected in Penn State's Stone Valley Forest,  
817 which is funded by the Penn State College of Agriculture Sciences, Department of  
818 Ecosystem Science and Management, and managed by the staff of the Forestlands  
819 Management Office.



## 820 References

- 821 Andrews, D. M., Lin, H., Zhu, Q., Jin, L., and Brantley, S. L.: Hot spots and hot moments of dissolved  
822 organic carbon export and soil organic carbon storage in the Shale Hills catchment,  
823 *Vadose Zone Journal*, 10, 943-954, 2011.
- 824 Anyah, R. O., Weaver, C. P., Miguez-Macho, G., Fan, Y., and Robock, A.: Incorporating water table  
825 dynamics in climate modeling: 3. Simulated groundwater influence on coupled land -  
826 atmosphere variability, *Journal of Geophysical Research: Atmospheres*, 113, 2008.
- 827 Bai, J., Zhang, G., Zhao, Q., Lu, Q., Jia, J., Cui, B., and Liu, X.: Depth-distribution patterns and  
828 control of soil organic carbon in coastal salt marshes with different plant covers, *Sci Rep -  
829 Uk*, 6, 34835, 10.1038/srep34835, 2016.
- 830 Bao, C., Li, L., Shi, Y., and Duffy, C.: Understanding watershed hydrogeochemistry: 1.  
831 Development of RT-Flux-PIHM, *Water Resources Research*, 53, 2328-2345, 2017.
- 832 Basu, N. B., Destouni, G., Jawitz, J. W., Thompson, S. E., Loukinova, N. V., Darracq, A., Zanardo, S.,  
833 Yaeger, M., Sivapalan, M., Rinaldo, A., and Rao, P. S. C.: Nutrient loads exported from  
834 managed catchments reveal emergent biogeochemical stationarity, *Geophys. Res. Lett.*,  
835 37, 10.1029/2010GL045168, 2010.
- 836 Bhatt, G., Kumar, M., and Duffy, C. J.: A tightly coupled GIS and distributed hydrologic modeling  
837 framework, *Environmental Modelling & Software*, 62, 70-84,  
838 10.1016/j.envsoft.2014.08.003, 2014.
- 839 Billen, G.: Etude écologique des transformations de l'azote dans les sédiments marins, 1977.
- 840 Brady, N. C., Weil, R. R., and Weil, R. R.: The nature and properties of soils, Prentice Hall Upper  
841 Saddle River, NJ, 2008.
- 842 Brantley, S. L., Kubicki, J. D., and White, A. F.: Kinetics of water-rock interaction, 2008.
- 843 Brantley, S. L., Lebedeva, M. I., Balashov, V. N., Singha, K., Sullivan, P. L., and Stinchcomb, G.:  
844 Toward a conceptual model relating chemical reaction fronts to water flow paths in hills,  
845 *Geomorphology*, 277, 100-117, 2017.
- 846 Brantley, S. L., White, T., West, N., Williams, J. Z., Forsythe, B., Shapich, D., Kaye, J., Lin, H., Shi, Y.,  
847 N., Kaye, M., Herndon, E., Davis, K. J., He, Y., Eissenstat, D., Weitzman, J., DiBiase, R., Li,  
848 L., Reed, W., Brubaker, K., and Gu, X.: Susquehanna Shale Hills Critical Zone Observatory:  
849 Shale Hills in the Context of Shaver's Creek Watershed, *Vadose Zone Journal*, 17, 1-19,  
850 ARTN 180092, 10.2136/vzj2018.04.0092, 2018.
- 851 Buysse, J., Smolders, E., and Merckx, R.: Modelling the uptake of nitrate by a growing plant with  
852 an adjustable root nitrate uptake capacity, *Plant and Soil*, 181, 19-23, 1996.
- 853 Cai, X., Yang, Z.-L., Fisher, J., Zhang, X., Barlage, M., and Chen, F.: Integration of nitrogen dynamics  
854 into the Noah-MP land surface model v1. 1 for climate and environmental predictions,  
855 *Geoscientific Model Development (Online)*, 9, 2016.
- 856 Chiou, C. T., Lee, J. F., and Boyd, S. A.: The surface area of soil organic matter, *Environmental  
857 Science & Technology*, 24, 1164-1166, 1990.
- 858 Condon, L. E., Maxwell, R. M., and Gangopadhyay, S.: The impact of subsurface conceptualization  
859 on land energy fluxes, *Advances in Water Resources*, 60, 188-203,  
860 10.1016/j.advwatres.2013.08.001, 2013.
- 861 Crawford, N. M., and Glass, A. D.: Molecular and physiological aspects of nitrate uptake in plants,  
862 *Trends in plant science*, 3, 389-395, 1998.



- 863 Davidson, E. A., and Janssens, I. A.: Temperature sensitivity of soil carbon decomposition and  
864 feedbacks to climate change, *Nature*, 440, 165-173, 10.1038/nature04514, 2006.
- 865 Davidson, E. A., Janssens, I.A.: Temperature sensitivity of soil carbon decomposition and  
866 feedbacks to climate change, *Nature*, 440, 165-173, 2006.
- 867 Devienne-Barret, F., Justes, E., Machet, J., and Mary, B.: Integrated control of nitrate uptake by  
868 crop growth rate and soil nitrate availability under field conditions, *Annals of Botany*, 86,  
869 995-1005, 2000.
- 870 Dingman, S. L.: *Physical hydrology*, Waveland press, 2015.
- 871 Dunbabin, V. M., Diggle, A. J., Rengel, Z., and Van Hugten, R.: Modelling the interactions between  
872 water and nutrient uptake and root growth, *Plant and Soil*, 239, 19-38, 2002.
- 873 Fatichi, S., Vivoni, E. R., Ogden, F. L., Ivanov, V. Y., Mirus, B., Gochis, D., Downer, C. W., Camporese,  
874 M., Davison, J. H., Ebel, B., Jones, N., Kim, J., Mascaro, G., Niswonger, R., Restrepo, P.,  
875 Rigon, R., Shen, C., Sulis, M., and Tarboton, D.: An overview of current applications,  
876 challenges, and future trends in distributed process-based models in hydrology, *Journal*  
877 *of Hydrology*, 537, 45-60, 10.1016/j.jhydrol.2016.03.026, 2016.
- 878 Fatichi, S., Manzoni, S., Or, D., and Paschalis, A.: A Mechanistic Model of Microbially Mediated  
879 Soil Biogeochemical Processes: A Reality Check, *Global Biogeochemical Cycles*, 33, 620-  
880 648, 10.1029/2018gb006077, 2019.
- 881 Filoso, S., Vallino, J., Hopkinson, C., Rastetter, E., and Claessens, L.: Modeling nitrogen transport  
882 in the Ipswich River Basin, Massachusetts, using a hydrological simulation program in  
883 FORTRAN (HSPF) 1, *JAWRA Journal of the American Water Resources Association*, 40,  
884 1365-1384, 2004.
- 885 Fisher, J., Sitch, S., Malhi, Y., Fisher, R., Huntingford, C., and Tan, S. Y.: Carbon cost of plant  
886 nitrogen acquisition: A mechanistic, globally applicable model of plant nitrogen uptake,  
887 retranslocation, and fixation, *Global Biogeochemical Cycles*, 24, 2010.
- 888 Friedlingstein, P., Cox, P., Betts, R., Bopp, L., von Bloh, W., Brovkin, V., Cadule, P., Doney, S., Eby,  
889 M., and Fung, I.: Climate–carbon cycle feedback analysis: results from the C4MIP model  
890 intercomparison, *Journal of climate*, 19, 3337-3353, 2006.
- 891 Gassman, P. W., Reyes, M. R., Green, C. H., and Arnold, J. G.: The soil and water assessment tool:  
892 Historical development, applications, and future research directions, *T Asabe*, 50, 1211-  
893 1250, 2007.
- 894 Gatel, L., Lauvernet, C., Carluer, N., Weill, S., Tournebize, J., and Paniconi, C.: Global evaluation  
895 and sensitivity analysis of a physically based flow and reactive transport model on a  
896 laboratory experiment, *Environmental Modelling & Software*, 113, 73-83,  
897 10.1016/j.envsoft.2018.12.006, 2019.
- 898 Gleeson, T., Befus, K. M., Jasechko, S., Luijendijk, E., and Cardenas, M. B.: The global volume and  
899 distribution of modern groundwater, *Nature Geoscience*, 9, 161, 10.1038/ngeo2590  
900 <https://www.nature.com/articles/ngeo2590#supplementary-information>, 2015.
- 901 Godsey, S. E., Kirchner, J. W., and Clow, D. W.: Concentration–discharge relationships reflect  
902 chemostatic characteristics of US catchments, *Hydrol. Process.*, 23, 1844-1864,  
903 10.1002/hyp.7315, 2009.
- 904 Green, T. R.: Linking climate change and groundwater, in: *Integrated groundwater management*,  
905 Springer, Cham, 97-141, 2016.
- 906 Gurdak, J. J.: Groundwater: Climate-induced pumping, *Nature Geoscience*, 10, 71, 2017.



- 907 Hachiya, T., and Sakakibara, H.: Interactions between nitrate and ammonium in their uptake,  
908 allocation, assimilation, and signaling in plants, *Journal of Experimental Botany*, 68, 2501-  
909 2512, 10.1093/jxb/erw449, 2016.
- 910 Hamamoto, S., Moldrup, P., Kawamoto, K., and Komatsu, T.: Excluded -volume expansion of  
911 Archie's law for gas and solute diffusivities and electrical and thermal conductivities in  
912 variably saturated porous media, *Water Resources Research*, 46, 2010.
- 913 Han, B., Benner, S. G., and Flores, A. N.: Including Variability across Climate Change Projections  
914 in Assessing Impacts on Water Resources in an Intensively Managed Landscape, *Water*,  
915 11, 286, 2019.
- 916 Hararuk, O., Smith, M. J., and Luo, Y.: Microbial models with data-driven parameters predict  
917 stronger soil carbon responses to climate change, *Glob. Chang. Biol.*, 21, 2439-2453,  
918 10.1111/gcb.12827, 2015.
- 919 Hasenmueller, E. A., Jin, L., Stinchcomb, G. E., Lin, H., Brantley, S. L., and Kaye, J. P.: Topographic  
920 controls on the depth distribution of soil CO<sub>2</sub> in a small temperate watershed, *Applied  
921 Geochemistry*, 63, 58-69, 2015.
- 922 Hasenmueller, E. A., Gu, X., Weitzman, J. N., Adams, T. S., Stinchcomb, G. E., Eissenstat, D. M.,  
923 Drohan, P. J., Brantley, S. L., and Kaye, J. P.: Weathering of rock to regolith: The activity of  
924 deep roots in bedrock fractures, *Geoderma*, 300, 11-31, 2017.
- 925 Heidari, P., Li, L., Jin, L., Williams, J. Z., and Brantley, S. L.: A reactive transport model for Marcellus  
926 shale weathering, *Geochimica et Cosmochimica Acta*, 217, 421-440, 2017.
- 927 Herndon, E. M., Dere, A. L., Sullivan, P. L., Norris, D., Reynolds, B., and Brantley, S. L.: Landscape  
928 heterogeneity drives contrasting concentration–discharge relationships in shale  
929 headwater catchments, *Hydrology and earth system sciences*, 19, 3333-3347, 2015.
- 930 Hindmarsh, A. C., Brown, P. N., Grant, K. E., Lee, S. L., Serban, R., Shumaker, D. E., and Woodward,  
931 C. S.: SUNDIALS: Suite of nonlinear and differential/algebraic equation solvers, *ACM  
932 Transactions on Mathematical Software (TOMS)*, 31, 363-396, 2005.
- 933 Hodges, C., Kim, H., Brantley, S. L., and Kaye, J.: Soil CO<sub>2</sub> and O<sub>2</sub> Concentrations Illuminate the  
934 Relative Importance of Weathering and Respiration to Seasonal Soil Gas Fluctuations, *Soil  
935 Science Society of America Journal*, 83, 1167-1180, 2019.
- 936 Jin, L., and Brantley, S. L.: Soil chemistry and shale weathering on a hillslope influenced by  
937 convergent hydrologic flow regime at the Susquehanna/Shale Hills Critical Zone  
938 Observatory, *Applied Geochemistry*, 26, Supplement, S51-S56,  
939 10.1016/j.apgeochem.2011.03.027, 2011.
- 940 Jin, L. X., Ravella, R., Ketchum, B., Bierman, P. R., Heaney, P., White, T., and Brantley, S. L.: Mineral  
941 weathering and elemental transport during hillslope evolution at the Susquehanna/Shale  
942 Hills Critical Zone Observatory, *Geochim Cosmochim Acta*, 74, 3669-3691,  
943 10.1016/j.gca.2010.03.036, 2010.
- 944 Kaiser, K., and Guggenberger, G.: Mineral surfaces and soil organic matter, *European Journal of  
945 Soil Science*, 54, 219-236, 10.1046/j.1365-2389.2003.00544.x, 2003.
- 946 Kirchner, J. W.: A double paradox in catchment hydrology and geochemistry, *Hydrol. Process.*, 17,  
947 871-874, 10.1002/hyp.5108, 2003.
- 948 Kuntz, B. W., Rubin, S., Berkowitz, B., and Singha, K.: Quantifying Solute Transport at the Shale  
949 Hills Critical Zone Observatory, *Vadose Zone Journal*, 10, 843-857, 10.2136/vzj2010.0130,  
950 2011.



- 951 Lam, Q. D., Schmalz, B., and Fohrer, N.: Modelling point and diffuse source pollution of nitrate in  
952 a rural lowland catchment using the SWAT model, *Agricultural Water Management*, 97,  
953 317-325, 10.1016/j.agwat.2009.10.004, 2010.
- 954 Laroche, A.-M., Gallichand, J., Lagacé, R., and Pesant, A.: Simulating atrazine transport with HSPF  
955 in an agricultural watershed, *Journal of Environmental Engineering*, 122, 622-630, 1996.
- 956 Leonard, L., and Duffy, C. J.: Essential terrestrial variable data workflows for distributed water  
957 resources modeling, *Environmental modelling & software*, 50, 85-96, 2013.
- 958 Li, L., Salehikhoo, F., Brantley, S. L., and Heidari, P.: Spatial zonation limits magnesite dissolution  
959 in porous media, *Geochimica et Cosmochimica Acta*, 126, 555-573,  
960 10.1016/j.gca.2013.10.051, 2014.
- 961 Li, L., Bao, C., Sullivan, P. L., Brantley, S., Shi, Y., and Duffy, C.: Understanding watershed  
962 hydrogeochemistry: 2. Synchronized hydrological and geochemical processes drive  
963 stream chemostatic behavior, *Water Resources Research*, 53, 2346-2367, 2017a.
- 964 Li, L., Maher, K., Navarre-Sitchler, A., Druhan, J., Meile, C., Lawrence, C., Moore, J., Perdril, J.,  
965 Sullivan, P., Thompson, A., Jin, L., Bolton, E. W., Brantley, S. L., Dietrich, W. E., Mayer, K.  
966 U., Steefel, C. I., Valocchi, A., Zachara, J., Kocar, B., McIntosh, J., Tutolo, B. M., Kumar, M.,  
967 Sonnenthal, E., Bao, C., and Beisman, J.: Expanding the role of reactive transport models  
968 in critical zone processes, *Earth-Science Reviews*, 165, 280-301,  
969 10.1016/j.earscirev.2016.09.001, 2017b.
- 970 Li, L., DiBiase, R. A., Del Vecchio, J., Marcon, V., Hoagland, B., Xiao, D., Wayman, C., Tang, Q., He,  
971 Y., Silverhart, P., Szink, I., Forsythe, B., Williams, J. Z., Shapich, D., Mount, G. J., Kaye, J.,  
972 Guo, L., Lin, H., Eissenstat, D., Dere, A., Brubaker, K., Kaye, M., Davis, K. J., Russo, T., and  
973 Brantley, S. L.: The Effect of Lithology and Agriculture at the Susquehanna Shale Hills  
974 Critical Zone Observatory, *Vadose Zone Journal*, 17, 10.2136/vzj2018.03.0063, 2018.
- 975 Li, L.: Watershed reactive transport, *Reviews in Mineralogy and Geochemistry*, 85, 381-418, 2019.
- 976 Lin, H.: Temporal stability of soil moisture spatial pattern and subsurface preferential flow  
977 pathways in the shale hills catchment, *Vadose Zone J*, 5, 317-340, 10.2136/vzj2005.0058,  
978 2006.
- 979 Maavara, T., Lauerwald, R., Laruelle, G. G., Akbarzadeh, Z., Bouskill, N. J., Van Cappellen, P., and  
980 Regnier, P.: Nitrous oxide emissions from inland waters: Are IPCC estimates too high?,  
981 *Global Change Biology*, 0, doi:10.1111/gcb.14504, 2018.
- 982 MacQuarrie, K. T. B., and Mayer, K. U.: Reactive transport modeling in fractured rock: A state-of-  
983 the-science review, *Earth-Science Reviews*, 72, 189-227, 10.1016/j.earscirev.2005.07.003,  
984 2005.
- 985 Marin-Spiotta, E., Silver, W. L., Swanston, C. W., and Ostertag, R.: Soil organic matter dynamics  
986 during 80 years of reforestation of tropical pastures, *Global Change Biology*, 15, 1584-  
987 1597, 10.1111/j.1365-2486.2008.01805.x, 2009.
- 988 Maxwell, R. M., Lundquist, J. K., Mirocha, J. D., Smith, S. G., Woodward, C. S., and Tompson, A. F.:  
989 Development of a coupled groundwater-atmosphere model, *Monthly Weather Review*,  
990 139, 96-116, 2011.
- 991 Mayer, K. U., Frind, E. O., and Blowes, D. W.: Multicomponent reactive transport modeling in  
992 variably saturated porous media using a generalized formulation for kinetically controlled  
993 reactions, *Water Resources Research*, 38, 13-11-13-21, 10.1029/2001wr000862, 2002.



- 994 Miller, M. P., Tesoriero, A. J., Hood, K., Terziotti, S., and Wolock, D. M.: Estimating Discharge and  
995 Nonpoint Source Nitrate Loading to Streams From Three End-Member Pathways Using  
996 High-Frequency Water Quality Data, *Water Resources Research*, 53, 10201-10216,  
997 10.1002/2017wr021654, 2017.
- 998 Miller, M. P., Capel, P. D., García, A. M., and Ator, S. W.: Response of Nitrogen Loading to the  
999 Chesapeake Bay to Source Reduction and Land Use Change Scenarios: A SPARROW -  
1000 Informed Analysis, *JAWRA Journal of the American Water Resources Association*, 56, 100-  
1001 112, 2020.
- 1002 Moatar, F., Abbott, B. W., Minaudo, C., Curie, F., and Pinay, G.: Elemental properties, hydrology,  
1003 and biology interact to shape concentration - discharge curves for carbon, nutrients,  
1004 sediment, and major ions, *Water Resources Research*, 53, 1270-1287, 2017.
- 1005 Monod, J.: The growth of bacterial cultures, *Annual review of microbiology*, 3, 371-394, 1949.
- 1006 Moriasi, D. N., Gowda, P. H., Arnold, J. G., Mulla, D. J., Ale, S., and Steiner, J. L.: Modeling the  
1007 impact of nitrogen fertilizer application and tile drain configuration on nitrate leaching  
1008 using SWAT, *Agricultural Water Management*, 130, 36-43, 10.1016/j.agwat.2013.08.003,  
1009 2013.
- 1010 Musolff, A., Schmidt, C., Selle, B., and Fleckenstein, J. H.: Catchment controls on solute export,  
1011 *Adv. Water Resour.*, 86, 133-146, 10.1016/j.advwatres.2015.09.026, 2015.
- 1012 Neitsch, S. L., Arnold, J. G., Kiniry, J. R., and Williams, J. R.: Soil and water assessment tool  
1013 theoretical documentation version 2009, Texas Water Resources Institute, 2011.
- 1014 Niu, J., and Phanikumar, M. S.: Modeling watershed-scale solute transport using an integrated,  
1015 process-based hydrologic model with applications to bacterial fate and transport, *Journal*  
1016 *of Hydrology*, 529, 35-48, 10.1016/j.jhydrol.2015.07.013, 2015.
- 1017 Ostle, N. J., Smith, P., Fisher, R., Woodward, F. I., Fisher, J. B., Smith, J. U., Galbraith, D., Levy, P.,  
1018 Meir, P., McNamara, N. P., and Bardgett, R. D.: Integrating plant-soil interactions into  
1019 global carbon cycle models, *Journal of Ecology*, 97, 851-863, 10.1111/j.1365-  
1020 2745.2009.01547.x, 2009.
- 1021 Ottoy, S., Elsen, A., Van De Vreken, P., Gobin, A., Merckx, R., Hermy, M., and Van Orshoven, J.:  
1022 An exponential change decline function to estimate soil organic carbon stocks and their  
1023 changes from topsoil measurements, *European Journal of Soil Science*, 67, 816-826, 2016.
- 1024 Porporato, A., D'odorico, P., Laio, F., and Rodriguez-Iturbe, I.: Hydrologic controls on soil carbon  
1025 and nitrogen cycles. I. Modeling scheme, *Advances in water resources*, 26, 45-58, 2003.
- 1026 Qiu, H., Niu, J., and Hu, B. X.: Quantifying the integrated water and carbon cycle in a data-limited  
1027 karst basin using a process-based hydrologic model, *Environmental Earth Sciences*, 78,  
1028 328, 2019.
- 1029 Qu, Y., and Duffy, C. J.: A semidiscrete finite volume formulation for multiprocess watershed  
1030 simulation, *Water Resour. Res.*, 43, W08419, 10.1029/2006wr005752, 2007.
- 1031 Rasmussen, C., Heckman, K., Wieder, W. R., Keiluweit, M., Lawrence, C. R., Berhe, A. A.,  
1032 Blankinship, J. C., Crow, S. E., Druhan, J. L., Hicks Pries, C. E., Marin-Spiotta, E., Plante, A.  
1033 F., Schädel, C., Schimel, J. P., Sierra, C. A., Thompson, A., and Wagai, R.: Beyond clay:  
1034 towards an improved set of variables for predicting soil organic matter content,  
1035 *Biogeochemistry*, 137, 297-306, 10.1007/s10533-018-0424-3, 2018.



- 1036 Regnier, P., and Steefel, C. I.: A high resolution estimate of the inorganic nitrogen flux from the  
1037 Scheldt estuary to the coastal North Sea during a nitrogen-limited algal bloom, spring  
1038 1995, *Geochimica et Cosmochimica Acta*, 63, 1359-1374, 10.1016/s0016-7037(99)00034-  
1039 4, 1999.
- 1040 Rutherford, D. W., Chiou, C. T., and Kile, D. E.: Influence of soil organic matter composition on  
1041 the partition of organic compounds, *Environmental science & technology*, 26, 336-340,  
1042 1992.
- 1043 Saha, D., Rau, B. M., Kaye, J. P., Montes, F., Adler, P. R., and Kemanian, A. R.: Landscape control  
1044 of nitrous oxide emissions during the transition from conservation reserve program to  
1045 perennial grasses for bioenergy, *GCB Bioenergy*, 9, 783-795, 10.1111/gcbb.12395, 2017.
- 1046 Scudeler, C., Pangle, L., Pasetto, D., Niu, G.-Y., Volkmann, T., Paniconi, C., Putti, M., and Troch, P.:  
1047 Multiresponse modeling of variably saturated flow and isotope tracer transport for a  
1048 hillslope experiment at the Landscape Evolution Observatory, *Hydrology and Earth  
1049 System Sciences*, 20, 4061-4078, 2016.
- 1050 Sebestyen, S. D., Ross, D. S., Shanley, J. B., Elliott, E. M., Kendall, C., Campbell, J. L., Dail, D. B.,  
1051 Fernandez, I. J., Goodale, C. L., and Lawrence, G. B.: Unprocessed Atmospheric Nitrate in  
1052 Waters of the Northern Forest Region in the US and Canada, *Environmental science &  
1053 technology*, 53, 3620-3633, 2019.
- 1054 Seibert, J., Grabs, T., Köhler, S., Laudon, H., Winterdahl, M., and Bishop, K.: Linking soil- and  
1055 stream-water chemistry based on a Riparian Flow-Concentration Integration Model,  
1056 *Hydrol. Earth Syst. Sci.*, 13, 2287-2297, 10.5194/hess-13-2287-2009, 2009.
- 1057 Shi, Y.: Development of a land surface hydrologic modeling and data assimilation system for the  
1058 study of subsurface-land surface interaction, 2012.
- 1059 Shi, Y., Davis, K. J., Duffy, C. J., and Yu, X.: Development of a coupled land surface hydrologic  
1060 model and evaluation at a critical zone observatory, *Journal of Hydrometeorology*, 14,  
1061 1401-1420, 2013.
- 1062 Shi, Y., Eissenstat, D. M., He, Y., and Davis, K. J.: Using a spatially-distributed hydrologic  
1063 biogeochemistry model with a nitrogen transport module to study the spatial variation of  
1064 carbon processes in a Critical Zone Observatory, *Ecological Modelling*, 380, 8-21, 2018.
- 1065 Skamarock, W., and Klemp, J.: A Description of the Advanced Research WRF Model Version 4.  
1066 Ncar Technical Notes, No, NCAR/TN-556+ STR, 2019.
- 1067 Steefel, C., Appelo, C., Arora, B., Jacques, D., Kalbacher, T., Kolditz, O., Lagneau, V., Lichtner, P.,  
1068 Mayer, K. U., and Meeussen, J.: Reactive transport codes for subsurface environmental  
1069 simulation, *Computational Geosciences*, 19, 445-478, 2015.
- 1070 Steefel, C. I., and Lasaga, A. C.: A coupled model for transport of multiple chemical species and  
1071 kinetic precipitation/dissolution reactions with application to reactive flow in single phase  
1072 hydrothermal systems, *American Journal of science*, 294, 529-592, 1994.
- 1073 Steimke, A. L., Han, B., Brandt, J. S., and Flores, A. N.: Climate change and curtailment: Evaluating  
1074 water management practices in the context of changing runoff regimes in a snowmelt-  
1075 dominated basin, *Water*, 10, 1490, 2018.
- 1076 Taylor, R. G., Scanlon, B., Döll, P., Rodell, M., Van Beek, R., Wada, Y., Longuevergne, L., Leblanc,  
1077 M., Famiglietti, J. S., and Edmunds, M.: Ground water and climate change, *Nature climate  
1078 change*, 3, 322, 2013.





- 1079 Thornton, P. E., Doney, S. C., Lindsay, K., Moore, J. K., Mahowald, N., Randerson, J. T., Fung, I.,  
1080 Lamarque, J. F., Feddema, J. J., and Lee, Y. H.: Carbon-nitrogen interactions regulate  
1081 climate-carbon cycle feedbacks: results from an atmosphere-ocean general circulation  
1082 model, *Biogeosciences*, 6, 2099-2120, 10.5194/bg-6-2099-2009, 2009.
- 1083 Todd, D. K., and Mays, L. W.: *Groundwater Hydrology*, Welly Inte, 2005.
- 1084 Trumbore, S. E.: Comparison of carbon dynamics in tropical and temperate soils using  
1085 radiocarbon measurements, *Global Biogeochemical Cycles*, 7, 275-290,  
1086 10.1029/93GB00468, 1993.
- 1087 van der Velde, Y., de Rooij, G. H., Rozemeijer, J. C., van Geer, F. C., and Broers, H. P.: Nitrate  
1088 response of a lowland catchment: On the relation between stream concentration and  
1089 travel time distribution dynamics, *Water Resources Research*, 46,  
1090 10.1029/2010wr009105, 2010.
- 1091 van der Velde, Y., Vercauteren, N., Jaramillo, F., Dekker, S. C., Destouni, G., and Lyon, S. W.:  
1092 Exploring hydroclimatic change disparity via the Budyko framework, *Hydrological  
1093 Processes*, 28, 4110-4118, 10.1002/hyp.9949, 2014.
- 1094 Weiler, M., and McDonnell, J. R. J.: Testing nutrient flushing hypotheses at the hillslope scale: A  
1095 virtual experiment approach, *J. Hydrol.*, 319, 339-356, 10.1016/j.jhydrol.2005.06.040,  
1096 2006.
- 1097 Weitzman, J. N., and Kaye, J. P.: Nitrogen Budget and Topographic Controls on Nitrous Oxide in a  
1098 Shale-Based Watershed, *Journal of Geophysical Research: Biogeosciences*, 123, 1888-  
1099 1908, 2018.
- 1100 Wen, H., Perdrial, J., Bernal, S., Abbott, B. W., Dupas, R., Godsey, S. E., Harpold, A., Rizzo, D.,  
1101 Underwood, K., and Adler, T.: Temperature controls production but hydrology controls  
1102 export of dissolved organic carbon at the catchment scale, 24, 945-966, 2020.
- 1103 Wieder, W. R., Grandy, A. S., Kallenbach, C. M., and Bonan, G. B.: Integrating microbial physiology  
1104 and physio-chemical principles in soils with the Mlcrobial-MIneral Carbon Stabilization  
1105 (MIMICS) model, *Biogeosciences*, 11, 3899-3917, 10.5194/bg-11-3899-2014, 2014.
- 1106 Wieder, W. R., Allison, S. D., Davidson, E. A., Georgiou, K., Hararuk, O., He, Y., Hopkins, F., Luo, Y.,  
1107 Smith, M. J., and Sulman, B.: Explicitly representing soil microbial processes in Earth  
1108 system models, *Global Biogeochemical Cycles*, 29, 1782-1800, 2015.
- 1109 Winter, T., Harvey, J., Franke, O., and Alley, W.: Natural processes of ground-water and surface-  
1110 water interaction, *Ground Water and Surface Water: A Single Resource*, US Geological  
1111 Survey Circular, 1139, 2-50, 1998.
- 1112 Yan, Z. F., Bond-Lamberty, B., Todd-Brown, K. E., Bailey, V. L., Li, S. L., Liu, C. Q., and Liu, C. X.: A  
1113 moisture function of soil heterotrophic respiration that incorporates microscale  
1114 processes, *Nature Communications*, 9, 10.1038/s41467-018-04971-6, 2018.
- 1115 Zarnetske, J. P., Bouda, M., Abbott, B. W., Saiers, J., and Raymond, P. A.: Generality of hydrologic  
1116 transport limitation of watershed organic carbon flux across ecoregions of the United  
1117 States, *Geophysical Research Letters*, 45, 11,702-711,711, 2018.
- 1118 Zhi, W., Li, L., Dong, W. M., Brown, W., Kaye, J., Steefel, C., and Williams, K. H.: Distinct Source  
1119 Water Chemistry Shapes Contrasting Concentration-Discharge Patterns, *Water Resources  
1120 Research*, 55, 4233-4251, 10.1029/2018wr024257, 2019.